



Collisionless energy transfer in kinetic turbulence: field–particle correlations in Fourier space

Tak Chu Li¹[†], Gregory G. Howes², Kristopher G. Klein³, Yi-Hsin Liu¹
and Jason M. TenBarge⁴

¹Department of Physics and Astronomy, Dartmouth College, Hanover, New Hampshire 03755, USA

²Department of Physics and Astronomy, University of Iowa, Iowa City, IA 52242, USA

³Lunar and Planetary Laboratory, University of Arizona, Tucson, AZ 85719, USA

⁴Department of Astrophysical Sciences, Princeton University, Princeton, NJ 08544, USA

(Received 12 April 2019; revised 1 July 2019; accepted 2 July 2019)

Turbulence is commonly observed in nearly collisionless heliospheric plasmas, including the solar wind and corona and the Earth's magnetosphere. Understanding the collisionless mechanisms responsible for the energy transfer from the turbulent fluctuations to the particles is a frontier in kinetic turbulence research. Collisionless energy transfer from the turbulence to the particles can take place reversibly, resulting in non-thermal energy in the particle velocity distribution functions (VDFs) before eventual collisional thermalization is realized. Exploiting the information contained in the fluctuations in the VDFs is valuable. Here we apply a recently developed method based on VDFs, the field–particle correlation technique, to a $\beta = 1$, solar-wind-like, low-frequency Alfvénic turbulence simulation with well-resolved phase space to identify the field–particle energy transfer in velocity space. The field–particle correlations reveal that the energy transfer, mediated by the parallel electric field, results in significant structuring of the VDF in the direction parallel to the magnetic field. Fourier modes representing the length scales between the ion and electron gyroradii show that energy transfer is resonant in nature, localized in velocity space to the Landau resonances for each Fourier mode. The energy transfer closely follows the Landau resonant velocities with varying perpendicular wavenumber k_{\perp} and plasma β . This resonant signature, consistent with Landau damping, is observed in all diagnosed Fourier modes that cover the dissipation range of the simulation.

Key words: astrophysical plasmas, plasma heating, space plasma physics

1. Introduction

Plasma turbulence is ubiquitous in the universe. In near-Earth collisionless plasmas – such as the solar corona, the solar wind and the Earth's magnetosphere – turbulence plays a fundamental role in the transport of energy from large fluid scales to small

[†] Email address for correspondence: tak.chu.li@dartmouth.edu

kinetic scales. This cascade of turbulence energy across scales is usually characterized by a power law in the energy spectrum of fluctuating quantities. A spectral break (change of the power law index) in the energy spectrum near the proton scale defines the transition into the dissipation range where the turbulence energy is converted into plasma heat and/or particle energization. How this process occurs remains a key subject of current kinetic plasma research in space observations (He *et al.* 2012; Alexandrova *et al.* 2013; Chen *et al.* 2013; Narita *et al.* 2016; Perrone *et al.* 2016; Roberts *et al.* 2017; Vech, Klein & Kasper 2017; Wang *et al.* 2018), numerical simulations (Howes *et al.* 2008*b*; Parashar *et al.* 2009; Karimabadi *et al.* 2013; TenBarge, Howes & Dorland 2013; Chang, Peter Gary & Wang 2014; Vásconez *et al.* 2014; Franci *et al.* 2015; Told *et al.* 2015; Li *et al.* 2016; Navarro *et al.* 2016; Parashar & Matthaeus 2016; Wan *et al.* 2016; Grošelj *et al.* 2017; Hughes *et al.* 2017; Yang *et al.* 2017; Cerri, Kunz & Califano 2018; Grošelj *et al.* 2018; Arzamasskiy *et al.* 2019; Kawazura, Barnes & Schekochihin 2019) and theoretical efforts (Howes *et al.* 2008*a*; Schekochihin *et al.* 2009; Boldyrev *et al.* 2013; Howes 2015; Passot & Sulem 2015; Schekochihin *et al.* 2016; Adkins & Schekochihin 2018; Schekochihin, Kawazura & Barnes 2019).

Recent advances in temporal and phase-space resolution in spacecraft observations (Servidio *et al.* 2017; Chen, Klein & Howes 2019) and numerical simulations (Li *et al.* 2016; Klein, Howes & TenBarge 2017; Cerri *et al.* 2018) have opened up new pathways for characterizing turbulence: using the velocity distribution functions (VDFs) to investigate non-thermal structures in the velocity space arising from the dissipation mechanisms. These velocity-space structures contain important information about the transfer of energy to particles from turbulent fields, ultimately leading to the thermodynamic heating of the plasma. Indeed, information in the VDFs underlying the nature of dissipation has been explored and identified in recent three-dimensional (3-D) kinetic turbulence simulations (Li *et al.* 2016; Klein *et al.* 2017; Cerri *et al.* 2018). Current space missions such as the Multiscale Magnetosphere Mission (MMS) (Burch *et al.* 2016) have the capability to sample well-resolved VDFs at high time cadence. Utilizing and understanding the crucial information contained in the phase space represents a new avenue in kinetic turbulence research (Howes 2017).

Recently, an innovative technique tracking the net energy transfer between turbulent fields and plasma particles in velocity space was developed, the field–particle correlation technique, (Klein & Howes 2016; Howes, Klein & Li 2017), and first illustrated in a nonlinear one-dimensional-one-velocity (1D–1V) Vlasov–Poisson plasma. Clear velocity-space signatures of direct energy exchange between the electric field and the particles was demonstrated. The 3-D implementation of this technique and application to single-point data sets was performed in gyrokinetic turbulence simulations, which showed velocity-space structures associated with ion Landau resonance (Klein *et al.* 2017). It was also applied to diagnose the particle energization in current sheets arising self-consistently from Alfvén wave collisions (Howes 2016), showing spatially localized energization by Landau damping (Howes, McCubbin & Klein 2018). It has recently been applied to well-resolved data from the MMS, which has provided evidence for electron Landau damping in the turbulent magnetosheath (Chen *et al.* 2019).

Both of these previous numerical studies sampled the 3-D electromagnetic turbulence simulation at single spatial points. Here we apply this technique in Fourier space for the first time. Sampling in Fourier space is a complementary approach to sampling in spatial space in numerical simulations, but it requires full spatial information of the system and therefore cannot be applied to spacecraft data that

often make *in situ* measurements from only one or a few spatial locations at a given time. Nevertheless, application of the field–particle correlation technique in Fourier space can be advantageous. It can be particularly useful in revealing information on the length scale dependence of the energy transfer mechanisms. In Alfvénic turbulence, the nonlinear turbulent cascade of Alfvén waves may undergo significant collisionless damping when it reaches the kinetic regime $k_{\perp}\rho_i \gtrsim 1$ (where k_{\perp} is the perpendicular wavenumber and ρ_i the ion gyroradius), where the kinetic Alfvén wave becomes dispersive. In this dispersive regime, the resonant velocity $v_{p\parallel}$ associated with the collisionless damping of kinetic Alfvén waves depends on k_{\perp} linearly. Sampling at a single point will measure contributions from a broad range of k_{\perp} modes, each with a different resonant velocity, potentially smearing out any resonant signatures of the energy transfer in velocity space. Analysing in Fourier space, however, each turbulent wave mode specified by $\mathbf{k} = (k_x, k_y, k_z)$ has $v_{p\parallel}$ that directly depends on k_{\perp} , producing a relatively clean resonant signature at that $v_{p\parallel}$ even in a turbulent plasma containing a broadband spectrum of modes.

In this work, we study the properties of energy transfer in a $\beta = 1$, gyrokinetic turbulence simulation. Resonant signatures associated with Landau resonances are observed in particle velocity space in all diagnosed Fourier modes spanning the dissipation range of the simulation. The energy transfer signatures also show a clear k_{\perp} dependence of the resonant velocity (moving to higher resonant velocities with increasing k_{\perp}), reflecting the characteristic of phase velocity of kinetic Alfvén waves. Remarkable agreement with the β dependence of the resonant velocity is observed in the energy transfer signatures in identical simulations with lower β . Our results demonstrate the resonant nature of field–particle energy transfer by collisionless wave–particle interactions with Alfvén waves.

This paper is organized as follows: the theory of nonlinear field–particle energy transfer in collisionless plasmas in three dimensions and in Fourier space is outlined in §2.1; field–particle correlations are defined and constructed in the gyrokinetic framework in §2.2; the form of field–particle correlations in Fourier space is derived in §2.3; the sampled spectrum in Fourier space is illustrated in §2.4; the simulation set-up and parameters are described in §2.5; the results on energy evolution of the systems are presented in §3; field–particle correlations in gyrotropic velocity space (v_{\parallel}, v_{\perp}) are examined in §4.1; primary results of this work including (i) examples of v_{\perp} -integrated, reduced correlations of individual Fourier modes for electrons and ions, (ii) correlations summing over a range of k_z modes for all diagnosed (k_x, k_y) Fourier modes, (iii) k_{\perp} dependence in summed- k_z modes and (iv) β_i dependence of energy transfer signatures are presented and discussed in §4.2; we further discuss and summarize our results in §5.

2. Techniques and simulation set-up

Here we describe the field–particle correlation technique in terms of its formulation in physical and Fourier space, its implementation within the gyrokinetic framework, and provide the set-up of the simulation.

2.1. Rate of energy transfer between fields and particles in a collisionless plasma

Dissipation in weakly collisional plasmas consists of a two-step process (Howes 2017). First, energy is transferred from the electromagnetic fields to plasma particles, appearing as non-thermal energy in the particle velocity distributions. This collisionless process is reversible. Then, the non-thermal energy is cascaded in phase

space, generating fine structures in the velocity space that are eventually smoothed out as thermal energy in the particle distributions via the action of collisions, and hence realizing irreversible heating of the plasma (Howes 2008; Schekochihin *et al.* 2008, 2009). The energy transfer directly measured by the field–particle correlation technique is the net energy transferred between the electromagnetic fields and plasma particles in the first step.

The theory describing the energy transfer between fields and plasma particles, which is directly measured in field–particle correlations, was first derived for a 1D–1V Vlasov–Poisson plasma (Klein & Howes 2016; Howes *et al.* 2017), and subsequently for a 3D–3V electromagnetic plasma (Klein *et al.* 2017). Here we briefly summarize the key points of the theory in 3D–3V, using insights from the 1D–1V model. Consider the Boltzmann’s equation for species $s(=i, e)$ in a proton–electron plasma

$$\frac{\partial f_s}{\partial t} + \mathbf{v} \cdot \nabla f_s + \frac{q_s}{m_s} \left(\mathbf{E} + \frac{\mathbf{v} \times \mathbf{B}}{c} \right) \cdot \frac{\partial f_s}{\partial \mathbf{v}} = \left(\frac{\partial f_s}{\partial t} \right)_c. \quad (2.1)$$

Focusing on the net collisionless energy transfer in the first step of dissipation, we neglect the collision term, $(\partial f_s / \partial t)_c$, on the right. We then multiply the whole equation by $m_s v^2 / 2$ to obtain an equation for the rate of change of phase-space energy density, $w_s \equiv (m_s v^2 / 2) f_s$,

$$\frac{\partial w_s}{\partial t} = -\mathbf{v} \cdot \nabla w_s - q_s \frac{v^2}{2} \mathbf{E} \cdot \frac{\partial f_s}{\partial \mathbf{v}} - \frac{q_s v^2}{c} (\mathbf{v} \times \mathbf{B}) \cdot \frac{\partial f_s}{\partial \mathbf{v}}. \quad (2.2)$$

When integrating over all space and velocity, w_s gives the microscopic kinetic energy W_s

$$W_s \equiv \int d^3 \mathbf{x} \int d^3 \mathbf{v} \frac{1}{2} m_s v^2 f_s. \quad (2.3)$$

When integrating (2.2) over all space, the first term on the right vanishes for periodic or infinite spatial boundaries. When integrating over velocity space, the magnetic force term involves $\mathbf{v} \cdot (\mathbf{v} \times \mathbf{B}) = 0$ and therefore does not contribute to the change of the microscopic kinetic energy W_s , as expected. The change of the microscopic kinetic energy, or equivalently, the energy transfer to species s , comes from the electric field term. We can further separate the E_{\parallel} and \mathbf{E}_{\perp} contributions to the rate of change of the microscopic kinetic energy as

$$\frac{\partial W_s}{\partial t} = -\frac{q_s}{2} \int d^3 \mathbf{x} \int d^3 \mathbf{v} v^2 \left(E_{\parallel} \frac{\partial f_s}{\partial v_{\parallel}} + \mathbf{E}_{\perp} \cdot \frac{\partial f_s}{\partial \mathbf{v}_{\perp}} \right), \quad (2.4)$$

where ‘ \parallel ’ is with respect to the local magnetic field. The first and second terms on the right represent energy transfer mediated by E_{\parallel} and \mathbf{E}_{\perp} , respectively. Note that this rate of energy density transfer, when integrated over velocity, simply yields the rate the work done by the electric field, $\mathbf{J}_s \cdot \mathbf{E} = J_{s\parallel} \cdot E_{\parallel} + \mathbf{J}_{s\perp} \cdot \mathbf{E}_{\perp}$ (Klein & Howes 2016; Howes *et al.* 2017; Klein *et al.* 2017).

2.2. Field–particle correlations and gyrokinetics

We can now construct the field–particle correlations based on (2.4). Without integrating over space or velocity, the transfer rate of phase-space energy density

can be directly computed by correlating E_{\parallel} or E_{\perp} with the corresponding velocity derivative of f_s at a point \mathbf{x} and time t over a correlation interval τ as

$$C_{E_{\parallel}}(\mathbf{x}, \mathbf{v}, t, \tau) = C \left(-q_s \frac{v_{\parallel}^2}{2} \frac{\partial f_s(\mathbf{x}, \mathbf{v}, t)}{\partial v_{\parallel}}, E_{\parallel}(\mathbf{x}, t) \right) \quad (2.5)$$

$$C_{E_{\perp}}(\mathbf{x}, \mathbf{v}, t, \tau) = C \left(-q_s \frac{v_{\perp 1}^2}{2} \frac{\partial f_s(\mathbf{x}, \mathbf{v}, t)}{\partial v_{\perp 1}}, E_{\perp 1}(\mathbf{x}, t) \right) + C \left(-q_s \frac{v_{\perp 2}^2}{2} \frac{\partial f_s(\mathbf{x}, \mathbf{v}, t)}{\partial v_{\perp 2}}, E_{\perp 2}(\mathbf{x}, t) \right), \quad (2.6)$$

where the unnormalized correlation on the right is defined as

$$C(A, B) = \frac{1}{N} \sum_{j=i+1}^{i+N} A_j B_j \quad (2.7)$$

for real quantities A_j and B_j measured at discrete times $t_j = j\Delta t$ over a correlation interval $\tau = N\Delta t$ that starts from an initial time t_{i+1} . The factor $v^2 = v_{\parallel}^2 + v_{\perp}^2$ in (2.4) is reduced to v_{\parallel}^2 in (2.5) upon integration $\int d\mathbf{v}_{\perp}$ as it can be separated from $\int d\mathbf{v}_{\parallel}$. The correlation interval τ is an important parameter in the unnormalized correlation. When τ is set to zero, the unnormalized correlation measures the instantaneous energy transfer at each time t , which often contains a large oscillatory component due to undamped wave motions. To measure the net secular or long-term energy transfer, τ is chosen to be sufficiently long such that the oscillatory component in the instantaneous energy transfer, which is often large but does not contribute to the net energy transfer, can be averaged out. Normally, one wave period of the outer-scale mode is sufficient (Howes *et al.* 2017). The parallel correlation $C_{E_{\parallel}}(\mathbf{x}, \mathbf{v}, t, \tau)$ measures the net energy transfer rate mediated by the parallel electric field, and is therefore a suitable measure for Landau damping (Landau 1946), or mechanisms like strong-guide-field magnetic reconnection that may be dominated by E_{\parallel} (Dahlin, Drake & Swisdak 2016); it, however, does not capture transit time damping (Barnes 1966; Quataert 1998) that arises from the change in the magnetic field strength. Similarly, the perpendicular correlation $C_{E_{\perp}}(\mathbf{x}, \mathbf{v}, t, \tau)$ captures the net transfer rate mediated by the perpendicular electric field, and is therefore suitable for determining cyclotron damping (Coleman 1968; Isenberg & Hollweg 1983) or stochastic ion heating (Chen, Lin & White 2001; Chandran *et al.* 2010). In this study using gyrokinetic simulations, we cannot explore perpendicular energization due to the conservation of the magnetic moment in gyrokinetic theory, so we focus here on the net energy transfer rate accomplished by E_{\parallel} .

In gyrokinetics, the system evolves in a three-spatial and two-velocity dimension (3D–2V) phase space, where the two velocity coordinates are v_{\parallel} and v_{\perp} . The distribution function to the first order in gyrokinetics (Howes *et al.* 2006) is given by

$$f_s(v_{\parallel}, v_{\perp}) = \left(1 - \frac{q_s \varphi}{T_{0s}} \right) F_{0s}(v) + h_s(v_{\parallel}, v_{\perp}), \quad (2.8)$$

where $F_{0s} = (n_{0s}/\pi^{3/2}v_{ts}^3) \exp(-v^2/v_{ts}^2)$ is the equilibrium Maxwellian distribution, $q_s\varphi/T_{0s}$ is the Boltzmann term (q_s the species charge and φ the electric potential), h_s is the first-order gyroaveraged part of the perturbed distribution. When substituting $f_s(v_{\parallel}, v_{\perp})$ into the first term in (2.4), we see that $\partial F_{0s}(v)/\partial v_{\parallel}$ is odd in v_{\parallel} , and is multiplied by an even power v_{\parallel}^2 . Thus, this term vanishes upon integration over all v_{\parallel} (again, $\int d\mathbf{v}_{\perp}$ can be separated from $\int d\mathbf{v}_{\parallel}$ here). Hence, the equilibrium Maxwellian distribution and the Boltzmann term in (2.8) do not contribute to the net

energy transfer in the field–particle correlation in (2.5). The perturbed, gyroaveraged contribution h_s can be used in place of f_s for the purpose of calculating field–particle correlations.

Another convenient transformation used is the complementary distribution function g_s (Schekochihin *et al.* 2009)

$$g_s(v_{\parallel}, v_{\perp}) = h_s(v_{\parallel}, v_{\perp}) - \frac{q_s F_{0s}}{T_{0s}} \left\langle \varphi - \frac{\mathbf{v}_{\perp} \cdot \mathbf{A}_{\perp}}{c} \right\rangle_{R_s}, \tag{2.9}$$

where $\langle \dots \rangle$ represents gyroaveraging at constant guiding centre R_s , capturing the perturbations to the Maxwellian distribution in the moving frame of Alfvén waves. It retains the parallel perturbations of $\delta f_s (\equiv f_s - F_{0s})$ in (2.8), and is therefore appropriate for calculating the net energy transfer. Note that the term $\langle \varphi - \mathbf{v}_{\perp} \cdot \mathbf{A}_{\perp}/c \rangle_{R_s}$ is independent of v_{\parallel} , and therefore yields zero upon integration $\int dv_{\parallel}$ when substituted into the first term in (2.4). Therefore, this term is the same, whether evaluated with h_s or g_s . As a result, the correlation $C_{E_{\parallel}}$ in (2.5), which is based on this term, is quantitatively similar using h_s or g_s , but g_s contains less additional terms and can more clearly reveal structures near the resonant velocity in the distribution functions themselves.

Here we will use g_s in the calculation of field–particle correlations, so the specific parallel field–particle correlation used to analyse the gyrokinetic turbulence simulations here takes the form

$$C_{E_{\parallel}}(\mathbf{x}, v_{\parallel}, v_{\perp}, t, \tau) = C \left(-q_s \frac{v_{\parallel}^2}{2} \frac{\partial g_s(\mathbf{x}, v_{\parallel}, v_{\perp}, t)}{\partial v_{\parallel}}, E_{\parallel}(\mathbf{x}, t) \right), \tag{2.10}$$

where E_{\parallel} is gyroaveraged. For simplicity, we refer to this form of parallel correlation that depends on gyrotropic velocity space $(v_{\parallel}, v_{\perp})$ as $C_{E_{\parallel}}(v_{\parallel}, v_{\perp}, t)$. The parallel reduced correlation $C_{E_{\parallel}}(v_{\parallel}, t)$, defined by integrating $C_{E_{\parallel}}(v_{\parallel}, v_{\perp}, t)$ over all v_{\perp} , is given by

$$C_{E_{\parallel}}(v_{\parallel}, t, \tau) = \int v_{\perp} dv_{\perp} C_{E_{\parallel}}(v_{\parallel}, v_{\perp}, t, \tau). \tag{2.11}$$

2.3. Field–particle correlations in Fourier space

To derive the appropriate form of the field–particle correlation in Fourier space, we first express the electric field at a single position \mathbf{x} by a Fourier series

$$\mathbf{E}(\mathbf{x}) = \sum_{\mathbf{k}} \mathbf{E}_{\mathbf{k}} e^{i\mathbf{k} \cdot \mathbf{x}}, \tag{2.12}$$

summed over all Fourier modes \mathbf{k} in a 3-D domain of volume L^3 . The particle velocity distribution function $f_s(\mathbf{x})$ is expressed similarly in terms of its Fourier coefficients $f_{s\mathbf{k}}$. The product of two real quantities $A(\mathbf{x})$ and $B(\mathbf{x})$ integrated over a volume L^3 can be converted to a sum over the product of the Fourier coefficients

$$\int d^3\mathbf{x} A(\mathbf{x})B(\mathbf{x}) = L^3 \sum_{\mathbf{k}} A_{\mathbf{k}}^* B_{\mathbf{k}} = L^3 \sum_{\mathbf{k}} A_{\mathbf{k}} B_{\mathbf{k}}^*, \tag{2.13}$$

where the complex Fourier coefficients $A_{\mathbf{k}}$ and $B_{\mathbf{k}}$ both satisfy the reality condition $A_{\mathbf{k}} = A_{-\mathbf{k}}^*$. Substituting these Fourier series into (2.4) and using this relation, we obtain

the rate of change of microscopic kinetic energy in terms of the Fourier coefficients of the electric field and particle distribution function,

$$\frac{\partial W_s}{\partial t} = \sum_{\mathbf{k}} \left(-\frac{q_s}{2}\right) L^3 \int d^3\mathbf{v} v^2 \left(E_{\parallel\mathbf{k}} \frac{\partial f_{s\mathbf{k}}^*}{\partial v_{\parallel}} + \mathbf{E}_{\perp\mathbf{k}} \cdot \frac{\partial f_{s\mathbf{k}}^*}{\partial \mathbf{v}_{\perp}} \right). \quad (2.14)$$

Without summing over all Fourier modes, the contribution to the change of particle energy from each Fourier mode \mathbf{k} is given by the summand, leading to the following forms of the field-particle correlations in Fourier space corresponding to (2.5) and (2.6):

$$C_{E_{\parallel}}(\mathbf{k}, \mathbf{v}, t, \tau) = C \left(-q_s \frac{v_{\parallel}^2}{2} \frac{\partial f_{s\mathbf{k}}^*(\mathbf{v}, t)}{\partial v_{\parallel}}, E_{\parallel\mathbf{k}}(t) \right) \quad (2.15)$$

$$C_{E_{\perp}}(\mathbf{k}, \mathbf{v}, t, \tau) = C \left(-q_s \frac{v_{\perp 1}^2}{2} \frac{\partial f_{s\mathbf{k}}^*(\mathbf{v}, t)}{\partial v_{\perp 1}}, E_{\perp 1\mathbf{k}}(t) \right) + C \left(-q_s \frac{v_{\perp 2}^2}{2} \frac{\partial f_{s\mathbf{k}}^*(\mathbf{v}, t)}{\partial v_{\perp 2}}, E_{\perp 2\mathbf{k}}(t) \right). \quad (2.16)$$

The discussion on using g_s in gyrokinetics in place of f_s , which is based on velocity integrals, applies also to the correlations in Fourier space (with the gyroaveraging operation $\langle \dots \rangle$ in (2.9) reduced to multiplications by Bessel functions (Howes *et al.* 2006; Numata *et al.* 2010)). The parallel correlation in (2.10) then becomes

$$C_{E_{\parallel}}(\mathbf{k}, v_{\parallel}, v_{\perp}, t, \tau) = C \left(-q_s \frac{v_{\parallel}^2}{2} \frac{\partial g_{s\mathbf{k}}^*(v_{\parallel}, v_{\perp}, t)}{\partial v_{\parallel}}, E_{\parallel\mathbf{k}}(t) \right). \quad (2.17)$$

This represents the net energy transfer rate in Fourier and gyrotropic velocity space. Together with the parallel reduced correlation in (2.11), it is the form of field-particle correlations we use in this work.

2.4. Diagnosing energy transfer in Fourier space

Previous studies have used the field-particle correlation technique at a single point in physical space to evaluate the energy transfer between fields and particles (Klein & Howes 2016; Howes 2017; Howes *et al.* 2017, 2018; Klein 2017; Klein *et al.* 2017; Chen *et al.* 2019). Here we diagnose the particle energization in Fourier space, where each Fourier mode \mathbf{k} is specified by a normalized wavevector ($k_x \rho_i, k_y \rho_i, k_z L_z / 2\pi$), where L_z is the system size in z . There are a number of advantages when applying field-particle correlations in Fourier space compared to physical space. First, by utilizing full spatial information of the whole domain as opposed to a single point, we can determine how the length scale of fluctuations, within the broadband turbulent spectrum, influences the collisionless field-particle energy transfer. Second, in the gyrokinetic limit $k_{\parallel} \ll k_{\perp}$, well justified for the anisotropic turbulence observed in the solar wind at kinetic scales (Sahraoui *et al.* 2010; Narita *et al.* 2011; Roberts, Li & Li 2013; Roberts, Li & Jeska 2015), the parallel phase velocity $v_{p\parallel} = \omega/k_{\parallel}$ of the linear wave modes depends only on the perpendicular wavenumber and the plasma parameters, $\bar{\omega} \equiv \omega/(k_{\perp} v_A) = v_{p\parallel}/v_A = \bar{\omega}(k_{\perp} \rho_i, \beta_i, T_i/T_e)$ (Howes *et al.* 2006). Therefore, the parallel phase velocity that governs resonant collisionless interactions is well defined for each mode \mathbf{k} in Fourier space. In contrast, at a single point in physical space, the dispersive nature of kinetic Alfvén waves (see figure 1) would lead to a range of resonant velocities, broadening the energy transfer signal and

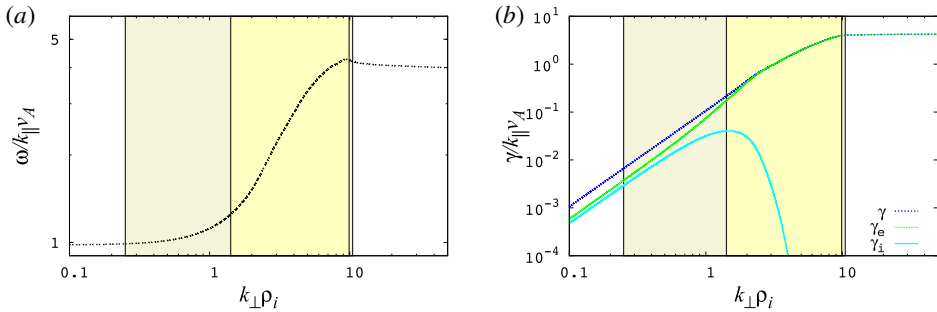


FIGURE 1. The linear gyrokinetic dispersion relation for a $\beta_i = 1$ and $T_i/T_e = 1$ plasma, showing (a) the normalized real frequency or phase velocity $\omega/k_{\parallel}v_A$ (dashed black) and (b) damping rates $\gamma/k_{\parallel}v_A$ for the electrons (green), ions (cyan) and the total damping rate (blue). The total shaded region represents the resolved dynamic range $0.25 \leq k_{\perp}\rho_i \leq 10.5$. The inner yellow shaded region indicates the range of the sampled k_{\perp} spectrum given in table 1, $1.4 \leq k_{\perp}\rho_i \leq 9.9$.

$(k_x\rho_i, k_y\rho_i)$	$k_{\perp}\rho_i$	$\omega/k_{\parallel}v_A = v_{p\parallel}/v_{ti}$	$v_{p\parallel}/v_{te}$	τ_k/τ_0
(1,1)	1.4	1.3	0.25	0.79
(2,2)	2.8	2.1	0.42	0.47
(3,4)	5.0	3.3	0.66	0.30
(5,5)	7.1	4.0	0.79	0.25
(6,6)	8.5	4.2	0.84	0.24
(7,7)	9.9	4.2	0.85	0.23

TABLE 1. List of diagnosed (k_x, k_y) modes in Fourier space.

potentially smearing out any resonant energy transfer signatures in velocity space. Third, the broadband turbulent fluctuations have decreasing amplitudes with increasing perpendicular wavenumber $k_{\perp}\rho_i$, but in Fourier space one can isolate the fluctuations at higher k_{\perp} from the rest of the fluctuations containing much larger amplitude fluctuations at lower k_{\perp} .

In figure 1, we plot (a) the normalized frequency $\omega/k_{\parallel}v_A$ and (b) the normalized damping rate $\gamma/k_{\parallel}v_A$ as a function of $k_{\perp}\rho_i$ from the linear gyrokinetic dispersion relation (Howes *et al.* 2006) for a plasma with parameters $\beta_i \equiv 8\pi n_i T_i / B^2 = v_{ti}^2 / v_A^2 = 1$, $T_i/T_e = 1$, and $m_i/m_e = 25$. The total shaded region represents the resolved dynamic range of k_{\perp} in the simulation, $0.25 \leq k_{\perp}\rho_i \leq 10.5$. Table 1 lists the perpendicular wavevectors $(k_x\rho_i, k_y\rho_i)$ of Fourier modes that are sampled in the simulation, along with the corresponding normalized perpendicular wavenumber $k_{\perp}\rho_i$, where $k_{\perp} \equiv \sqrt{k_x^2 + k_y^2}$. The range of these sampled perpendicular wavenumbers $k_{\perp}\rho_i$ is indicated in figure 1 by the inner yellow shaded region, covering $1.4 \leq k_{\perp}\rho_i \leq 9.9$ or $0.3 \leq k_{\perp}\rho_e \leq 2.0$. For each $(k_x\rho_i, k_y\rho_i)$ mode, seven $k_z L_z / 2\pi \in [-3, 3]$ modes are selected, for a total sampling of 42 modes in $(k_x\rho_i, k_y\rho_i, k_z L_z / 2\pi)$ Fourier space. Also tabulated in table 1 are the parallel phase velocities normalized to the ion thermal velocity, $v_{p\parallel}/v_{ti} = \omega/k_{\parallel}v_A$ (valid for a $\beta_i = 1$ plasma) and $v_{p\parallel}/v_{te}$. The last column gives the linear wave period τ_k of a kinetic Alfvén wave specified by $k_{\perp}\rho_i$.

The dispersion relation plot in figure 1(a) shows the characteristic dispersion of kinetic Alfvén waves, where the parallel phase velocity begins increasing at the

transition of $k_{\perp}\rho_i \sim 1$. Given the energy transfer from fields to particles due to resonant collisionless wave damping is governed by the parallel phase velocity, one would expect to observe that the region of velocity space in which the particles exchange energy with the fields, known as the velocity-space signature of the particle energization, will shift to higher parallel velocities, tracking the increased parallel phase velocity as the perpendicular wavenumber $k_{\perp}\rho_i$ increases. Our analysis in §§ 4.1 and 4.2 confirms this expectation.

Finally, the collisionless damping rates for ions (cyan) and electrons (green) and the total damping rate (blue) are plotted in figure 1(b). The total damping of the waves is primarily attributed to electron damping for $k_{\perp}\rho_i > 2$ while both ion and electron damping contribute for $k_{\perp}\rho_i < 2$. Particularly, ion collisionless damping becomes significant and peaks around $k_{\perp}\rho_i \sim 1$, but drops off very rapidly for $k_{\perp}\rho_i > 2$.

2.5. Simulation set-up

The simulation was performed with the gyrokinetic code AstroGK (Numata *et al.* 2010). It has been extensively used to investigate turbulence in weakly collisional space plasmas (Howes *et al.* 2008*b*; Tatsuno *et al.* 2009; Howes *et al.* 2011; TenBarge & Howes 2012; Nielson, Howes & Dorland 2013; TenBarge & Howes 2013; Kobayashi, Rogers & Numata 2014; Howes 2016; Li *et al.* 2016; Howes *et al.* 2018) as well as collisionless magnetic reconnection in the strong-guide-field limit (Numata *et al.* 2011; TenBarge *et al.* 2014; Numata & Loureiro 2015). AstroGK is an Eulerian continuum code with triply periodic boundary conditions. It has a slab geometry elongated along the straight, uniform background magnetic field, $\mathbf{B}_0 = B_0\hat{z}$. The code evolves the perturbed gyroaveraged Vlasov–Maxwell equations in five-dimensional phase space (3D–2V) (Frieman & Chen 1982; Howes *et al.* 2006). The evolved quantities are the electromagnetic gyroaveraged complementary distribution function $g_s(x, y, z, \lambda, \varepsilon)$ for each species s , the scalar potential φ , parallel vector potential A_{\parallel} and the parallel magnetic field perturbation δB_{\parallel} , where \parallel is along the total local magnetic field $\mathbf{B} = B_0\hat{z} + \delta\mathbf{B}$. Note that the total and background magnetic fields are the same to first-order accuracy, which is retained for perturbed fields in gyrokinetics. The 2V velocity grid is specified by pitch angle $\lambda = v_{\perp}^2/v^2$ and energy $\varepsilon = v^2/2$. The background distribution functions for both species are stationary uniform Maxwellians. Collisions are incorporated using a fully conservative, linearized gyroaveraged Landau collision operator consisting of energy diffusion and pitch-angle scattering between like particles, electrons and ions and inter-species scattering of electrons off ions (Abel *et al.* 2008; Barnes *et al.* 2009).

The same simulation set-up as Li *et al.* (2016) is used, a 3-D generalization of the classic 2-D Orszag–Tang Vortex (OTV) problem (Orszag & Tang 1979). The 2-D problem was widely used in fluid and MHD turbulence simulations; various 3-D generalizations have also been used for studying turbulence (Dahlburg & Picone 1989; Politano, Pouquet & Sulem 1989; Picone & Dahlburg 1991; Politano, Pouquet & Sulem 1995; Grauer & Marliani 2000; Mininni, Pouquet & Montgomery 2006; Parashar *et al.* 2009; Parashar, Vasquez & Markovskii 2014). This 3-D OTV set-up consists of counterpropagating Alfvén waves along $\mathbf{B} = B_0\hat{z}$ such that on the $z = 0$ plane, its initial condition reduces to that of the 2-D OTV problem. An initial amplitude z_0 of Elsässer variables in the OTV set-up (Li *et al.* 2016) is chosen to yield a nonlinearity parameter $\chi = k_{\perp}z_0/(k_{\parallel}v_A) = 1$ (where $v_A = B_0/\sqrt{4\pi m_i n_0}$ is a characteristic Alfvén speed), corresponding to critical balance (Goldreich & Sridhar 1995), or a state of strong turbulence. Note that previous studies using AstroGK

have shown consistency with the prediction of a critically balanced cascade in the dissipation range (TenBarge & Howes 2012; TenBarge *et al.* 2013).

To resolve the turbulent cascade from the inertial range to the dissipation range for both ions and electrons, a reduced mass ratio of $m_i/m_e = 25$ is used. The simulation domain is $L_\perp = 8\pi\rho_i$ and dimensions are $(n_x, n_y, n_z, n_\lambda, n_\varepsilon, n_s) = (128, 128, 32, 64, 32, 2)$, which resolves a dynamic range of $0.25 \leq k_\perp\rho_i \leq 10.5$, or $0.05 \leq k_\perp\rho_e \leq 2.1$, covering both the inertial and dissipation ranges of the system. Typical conditions of solar wind turbulence are considered with ion plasma beta $\beta_i = 8\pi n_i T_{0i}/B_0^2 = 1$, where T_{0i} is the constant background ion temperature, and equal temperatures are used for ions and electrons ($T_{0i}/T_{0e} = 1$).

To realize collisional dissipation of turbulent energy in particle velocity space, weak finite collision frequencies are required (Howes 2008; Schekochihin *et al.* 2008, 2009). Low collision frequencies $\nu_s/\omega_{A0} \ll 1$ are chosen to avoid altering the weakly collisional dynamics, where collision frequencies of $\nu_i = 3 \times 10^{-3}\omega_{A0}$ and $\nu_e = 0.06\omega_{A0}$ (where $\omega_{A0} \equiv k_\parallel v_A$ is a characteristic Alfvén wave frequency) are used. We also employ a constant ion hypercollision frequency of $\nu_{Hi} = 6 \times 10^{-3}\omega_{A0}$ and adaptive electron hypercollision frequency of $\nu_{He} = 0.12\omega_{A0}$ to ensure fluctuations in velocity space remain well resolved (Howes 2008; Howes *et al.* 2011). The electron hypercollisional coefficient is adjusted based on nonlinear estimations of the total collisional damping rate (including hypercollisions) γ_{nl} and of the energy transfer frequency ω_{nl} (that is given by the cascade model (Howes *et al.* 2008a) and dependent on the magnitude of the magnetic field fluctuations) such that a value of $\gamma_{nl}/\omega_{nl} \simeq 1/2\pi$ is achieved within some tolerance. The hypercollisionality chosen has the form of a pitch-angle-scattering operator with a wavenumber-dependent collision rate $\nu_{Hs}(k_\perp/k_{\perp\max})^{p_s}$, where $k_{\perp\max}$ is a grid-scale wavenumber with $p_i = 4$ and $p_e = 8$. It produces positive-definite heating close to the grid scale and is sufficient to terminate the turbulent cascade at the smallest resolved scales.

3. Energy evolution and current density

Here we present an overview of the evolution of the 3-D OTV simulation in terms of the evolution of the energy and the self-consistent development of current sheets in the simulation.

Under weakly collisional conditions, the removal of energy from turbulent fluctuations and the eventual conversion of that energy into plasma heat, unlike in the more familiar fluid limit, is a two-step process (Howes 2017): first, the turbulent fluctuations are damped through reversible, collisionless interactions between the electromagnetic fields and the plasma particles, leading to energization of the particles; and second, this non-thermal energization of the particle velocity distributions is subsequently thermalized by arbitrarily weak collisions, thereby accomplishing the ultimate conversion of the turbulent energy into particle heat.

In a gyrokinetic system, the total fluctuating energy δW (Howes *et al.* 2006; Brizard & Hahn 2007; Schekochihin *et al.* 2009) is given by¹

$$\delta W = \int d^3\mathbf{r} \left[\frac{|\delta\mathbf{B}|^2 + |\delta\mathbf{E}|^2}{8\pi} + \sum_s \int d^3\mathbf{v} \frac{T_{0s}\delta f_s^2}{2F_{0s}} \right], \quad (3.1)$$

where the index s indicates the plasma species and T_{0s} is the temperature of each species' Maxwellian equilibrium. The left term represents the electromagnetic energy

¹Note that in the gyrokinetic approximation, the electric field energy is relativistically small relative to the magnetic field energy (Howes *et al.* 2006).

and the right term represents that microscopic fluctuating kinetic energy of the particles of each plasma species s . As explained in Howes *et al.* (2018), in the standard form of gyrokinetic theory the appropriate conserved quadratic quantity in gyrokinetics is the Kruskal–Obermann energy, $E_s^{(\delta f)} \equiv \int d^3\mathbf{r} \int d^3\mathbf{v} T_{0s} \delta f_s^2 / 2F_{0s}$ (Kruskal & Oberman 1958; Morrison 1994), in contrast to the usual kinetic theory definition of microscopic kinetic energy, $\int d^3\mathbf{r} \int d^3\mathbf{v} (m_s v^2 / 2) f_s$. Note also that δW includes neither the equilibrium thermal energy, $\int d^3\mathbf{r} (3/2) n_{0s} T_{0s} = \int d^3\mathbf{r} \int d^3\mathbf{v} 1/2 m_s v^2 F_{0s}$, nor the equilibrium magnetic field energy, $\int d^3\mathbf{r} B_0^2 / 8\pi$. Thus, the terms of δW in (3.1) represent the perturbed electromagnetic field energies and the microscopic kinetic energy of the deviations from the Maxwellian velocity distribution for each species.

A more intuitive form of the total fluctuating energy δW can be obtained by separating out the kinetic energy of the bulk motion of the plasma species from the non-thermal energy in the distribution function that is not associated with bulk flows (Li *et al.* 2016),

$$\delta W = \int d^3\mathbf{r} \left[\frac{|\delta\mathbf{B}|^2 + |\delta\mathbf{E}|^2}{8\pi} + \sum_s \left(\frac{1}{2} n_{0s} m_s |\delta\mathbf{u}_s|^2 + \frac{3}{2} \delta P_s \right) \right], \quad (3.2)$$

where n_{0s} is the equilibrium density, m_s is mass and $\delta\mathbf{u}_s$ is the fluctuating bulk flow velocity, which includes the parallel and perpendicular bulk flows. The non-thermal energy in the distribution function (not including the bulk kinetic energy) is defined by TenBarge *et al.* (2014)

$$E_s^{(nt)} \equiv \int d^3\mathbf{r} \frac{3}{2} \delta P_s \equiv \int d^3\mathbf{r} \left[\int d^3\mathbf{v} \left(\frac{T_{0s} \delta f_s^2}{2F_{0s}} \right) - \frac{1}{2} n_{0s} m_s |\delta\mathbf{u}_s|^2 \right]. \quad (3.3)$$

The turbulent energy is defined as the sum of the electromagnetic field and the bulk flow kinetic energies (Howes 2015; Li *et al.* 2016; Howes *et al.* 2018),

$$E^{(turb)} \equiv \int d^3\mathbf{r} \left[\frac{|\delta\mathbf{B}|^2 + |\delta\mathbf{E}|^2}{8\pi} + \sum_s \frac{1}{2} n_{0s} m_s |\delta\mathbf{u}_s|^2 \right]. \quad (3.4)$$

Therefore the total fluctuating energy is simply the sum of the turbulent energy and species non-thermal energies, $\delta W = E^{(turb)} + E_i^{(nt)} + E_e^{(nt)}$.

In figure 2, we present area plots of the components of the energy in the simulation as a function of normalized time t/τ_0 , where τ_0 is the period of Alfvén waves at the domain scale. Note that collisions in AstroGK, as well as in real plasma systems, convert non-thermal to thermal energy, representing irreversible plasma heating with an associated increase of entropy. The energy lost from δW by collisions is tracked by AstroGK and represents thermal heating of the plasma species, but this energy is not fed back into the code to evolve the equilibrium thermal temperature, T_{0s} (Howes *et al.* 2006; Numata *et al.* 2010; Li *et al.* 2016). We account for the energy lost from δW in the AstroGK simulation to collisional plasma heating by accumulating the thermalized energy in each species over time, $E_s^{(\text{coll})}(t) = \int_0^t dt' Q_s(t')$, where AstroGK computes the collisional heating rate per unit volume for ions Q_i and electrons Q_e .

In figure 2(a), we plot the evolution of the energy budget over the course of the simulation, showing that turbulent energy $E^{(turb)}$, which dominates at the beginning of the simulation, is largely converted to electron heat $E_e^{(\text{coll})}$ and ion heat $E_i^{(\text{coll})}$ and by the end of the simulation, with approximately 70% of the initial total fluctuating energy δW_0 lost by $t/\tau_0 = 3$. Approximately one third of the energy dissipated is channelled to ions and two thirds to electrons. This is in close agreement with a

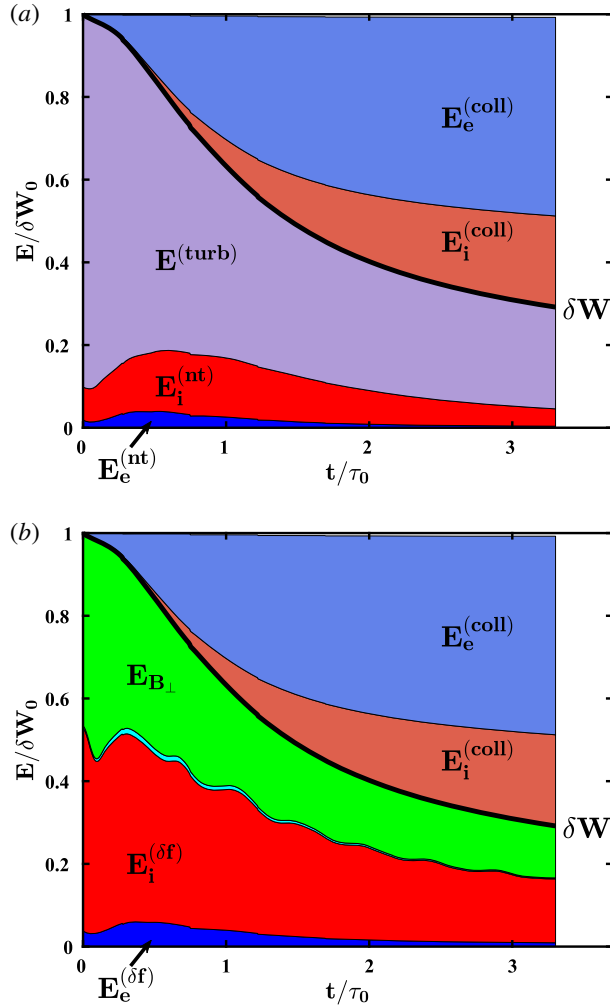


FIGURE 2. (a) The energy budget of the simulation versus time, showing the turbulent energy $E^{(turb)}$, non-thermal ion energy $E_i^{(nt)}$, non-thermal electron energy $E_e^{(nt)}$, ion heat $E_i^{(coll)}$ and electron heat $E_e^{(coll)}$. (b) The same energy budget decomposed according to (3.1), showing the perpendicular magnetic field energy $E_{B\perp}$, parallel magnetic field energy $E_{B\parallel}$ (cyan, not labelled, appearing between $E_{B\perp}$ and $E_i^{(\delta f)}$), total fluctuating ion kinetic energy $E_i^{(\delta f)}$, total fluctuating electron kinetic energy $E_e^{(\delta f)}$, ion heat $E_i^{(coll)}$ and electron heat $E_e^{(coll)}$. The total fluctuating energy δW is shown in both panels (thick black line).

recent gyrokinetic turbulent simulation using a realistic mass ratio of $m_i/m_e = 1836$ in which approximately 70% of the total dissipated energy is channelled through electrons (Told *et al.* 2015). Total energy E is conserved over the course of the simulation to less than 1%.

Another view of the energy budget, based on (3.1), is presented in figure 2(b), where we plot the perpendicular magnetic field energy $E_{B\perp}$ (green) and parallel magnetic field energy $E_{B\parallel}$ (cyan) along with the total fluctuating kinetic energy of the ions and electrons $E_s^{(\delta f)}$. An interesting feature of the evolution of the energy budget,

seen in both panels (*a,b*), is that although the electrons gain the bulk of the thermal energy, the total fluctuating kinetic energy $E_e^{(\delta f)}$ and total non-thermal energy $E_e^{(nt)}$ in the electrons remains small. Thus, electrons do not contain much of the non-thermal energy at any given time, and are an effective conduit for channelling the turbulent energy into electron thermal energy.

The field–particle correlation technique diagnoses the collisionless, reversible transfer of energy between the electromagnetic fields and the particles. This first step of the two-step process in converting turbulent energy into particle thermal energy is not easily discerned in the energy budget plots shown in figure 2. To more directly evaluate this rate of energy transfer, we compute the net rate of energy transfer due to field–particle interactions using

$$\dot{E}_s^{(fp)} = \dot{E}_s^{(nt)} + Q_s, \quad (3.5)$$

where $\dot{E}_s^{(nt)}$ is the rate of change of non-thermal species energy and Q_s is the collisional heating of the species. To check the energy conservation in the simulation, we can plot

$$-\dot{E}^{(turb)} = \dot{E}_i^{(fp)} + \dot{E}_e^{(fp)}, \quad (3.6)$$

because the rate of change of turbulent energy must be the sum of the collisionless field–particle energy transfer for each species.

In figure 3, we plot these energy transfer rates, normalized to the characteristic heating rate per unit volume, $Q_0 = (n_{0i}T_{0i}v_{ti}/L_{\parallel})(\pi/8)(L_{\perp}/L_{\parallel})^2$, for (*a*) ions (red) and (*b*) electrons (blue), as well as (*c*) the total energy transfer rate balance given by (3.6). Several features of these energy transfer rate curves are notable. First, with the exception of a brief large energy transfer to ions within the first $0.2\tau_0$, the field–particle energy transfer rate to electrons is about twice of that to ions on average. Second, the time lag between field–particle energy transfer to electrons and the collisional thermalization of that energy is very short, a delay of approximately $0.1\tau_0$. Thus, energy transferred to electron non-thermal energy is rapidly converted to electron heat by collisions. In contrast, for the ions, the time lag between the peaks of the field–particle energization of the ions and the collisional thermalization of that energy is much longer, approximately $1.0\tau_0$. This longer time lag for ions is consistent with the need for the ion entropy cascade (Schekochihin *et al.* 2009; Tatsuno *et al.* 2009; Cerri *et al.* 2018) to transfer non-thermal energy to sufficient small scales in velocity space before collisions can effectively thermalize that energy. Finally, (*c*) the sum of the field–particle energy transfer to ions and electrons is in quantitative agreement with the loss of turbulent energy.

In figure 4, we plot the spatial profiles on the $z=0$ plane at $t/\tau_0=0.5$ of (*a*) the parallel current J_{\parallel} (colour) and vector potential A_{\parallel} (contour), (*b*) $J_{\parallel}E_{\parallel}$ and (*c*) E_{\parallel} . The topology of the initial double-vortex pattern, representative of the Orzag–Tang vortex, is traceable by the central white contours. Multiscale features in J_{\parallel} , including self-consistently generated current sheets, are seen over the entire (x, y) plane, representing a turbulent state containing a spectrum of nonlinearly generated modes. $J_{\parallel}E_{\parallel}$ represents the net energy density transfer rate mediated by the parallel electric field (the first term on the right-hand side of (2.4) when integrated over velocity). In (*b*), strong energy transfer density (red) occurs in sub-ion- or ion-scale regions. Two particularly strong $J_{\parallel}E_{\parallel}$ regions are centred at $(x, y) \sim (3, 14)$ and $(20, 10)$. They co-locate with thin sheet-like currents and share similar shapes with them, but not necessarily with the strongest J_{\parallel} regions. They, however, are seen at the strongest E_{\parallel}

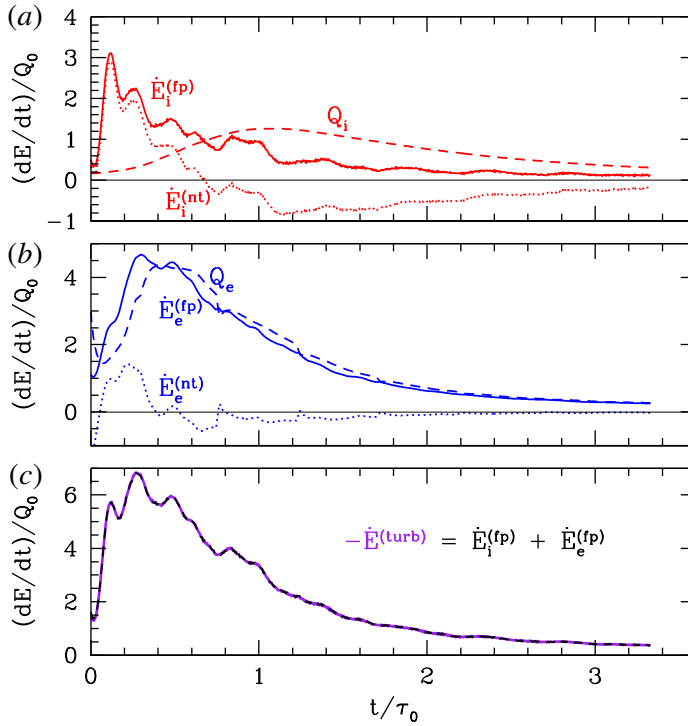


FIGURE 3. The rate of energy transfer by field–particle interactions $\dot{E}_s^{(fp)}$ (solid), the rate of change of non-thermal energy $\dot{E}_s^{(nt)}$ (dotted) and the collisional heating rate Q_s (dashed) for (a) ions (red) and (b) electrons (blue). (c) The energy balance between the loss of turbulent energy $-\dot{E}^{(turb)}$ (purple solid) and the summed transfer of energy to both ions and electrons, $\dot{E}_i^{(fp)} + \dot{E}_e^{(fp)}$ (black dashed).

in (c), which also occurs in localized ion-scale regions. Otherwise, E_{\parallel} has generally broad features.

4. Field–particle correlations

Here we present results on identifying the collisionless energy transfer in the simulation using field–particle correlations.

4.1. Field–particle correlations in gyrotropic velocity space

To identify the regions of gyrotropic velocity space (v_{\parallel} , v_{\perp}) where particles play a role in the collisionless transfer of energy density from the parallel electric field to the plasma ions and electrons, we employ the field–particle correlation technique to compute $C_{E_{\parallel}}(\mathbf{k}, v_{\parallel}, v_{\perp}, t, \tau)$, given by (2.17).

4.1.1. Electron gyrotropic correlations

Here we explore the net energy transfer rate to the electrons by the parallel electric field as a function of particle velocity in gyrotropic velocity space (v_{\parallel} , v_{\perp}) for particular Fourier modes, each denoted by their normalized wavevector ($k_x \rho_i, k_y \rho_i, k_z L_z / 2\pi$). On the top row of figure 5, we plot the instantaneous correlation $C_{E_{\parallel}}(\mathbf{k}, v_{\parallel}, v_{\perp}, t, \tau = 0)$ for modes (a) (2, 2, -1) and (b) (6, 6, +3). The instantaneous energy transfer is spread over a wide range of v_{\parallel} relative to $v_{p\parallel}$ of each Fourier mode of the kinetic

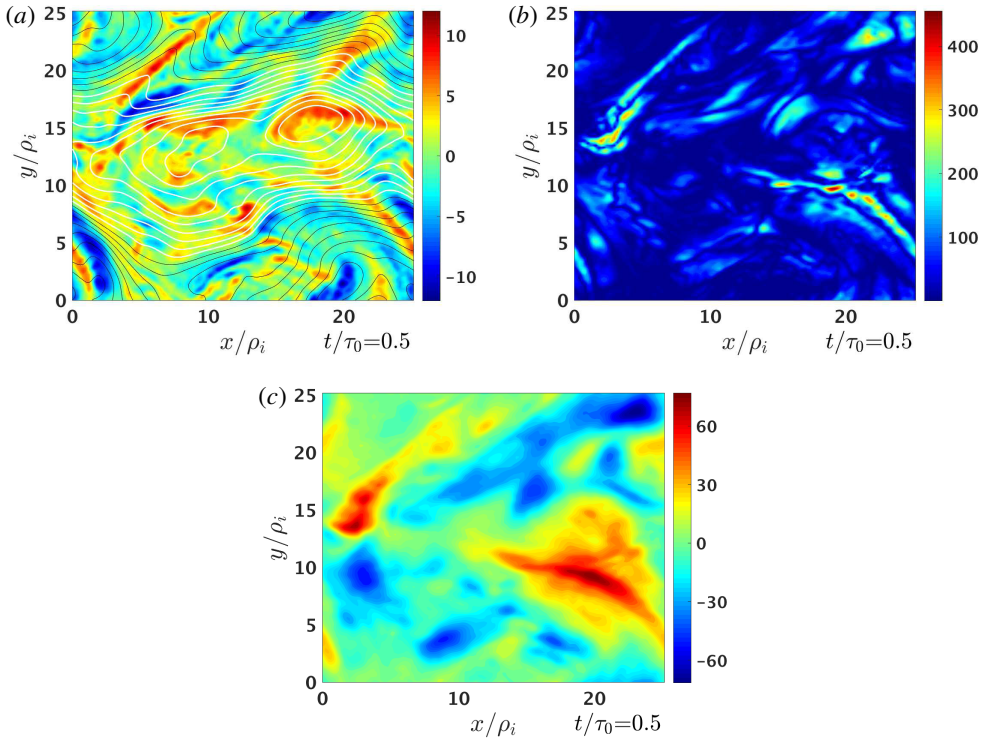


FIGURE 4. Spatial profile of (a) J_{\parallel} (colour) and A_{\parallel} (contour), (b) $J_{\parallel} E_{\parallel}$ and (c) E_{\parallel} on the $z = 0$ plane at $t/\tau_0 = 0.5$. Contours represent positive (white) and negative (black) values of A_{\parallel} .

Alfvén wave, given by (a) $\omega/(k_{\parallel} v_{te}) = \pm 0.42$ and (b) $\omega/(k_{\parallel} v_{te}) = \pm 0.84$, indicated by the vertical dashed black lines. This shows that particles over a relatively broad range of v_{\parallel} participate in energy exchange with the parallel electric field.

In order to eliminate the often large contribution to the instantaneous energy transfer given by the oscillating energy transfer associated with undamped wave motions (which is measured in a kinetic Alfvén wave (Gershman *et al.* 2017)), the field–particle correlation technique performs a time average of the correlation product (in the unnormalized correlation) over a suitably long time period (Klein & Howes 2016; Howes *et al.* 2017). This effectively removes the oscillating component of the energy transfer, isolating the often smaller net secular energy transfer from fields to particles. In both of these cases, we choose a correlation interval $\tau = 2\tau_k$ where τ_k is the linear wave period of a kinetic Alfvén wave specified by the normalized wavevector, given by the final column in table 1. The correlation interval is chosen such that the time evolution of the parallel reduced correlation qualitatively converges, which corresponds to $\tau \geq \tau_k$ (see Appendix). The resulting time-averaged field–particle correlations are plotted in figure 5 for Fourier modes (c) (2, 2, -1) and (d) (6, 6, +3).

For the time-averaged correlations, time t is defined at the beginning of the correlation interval τ . Another convenient way to specify time is at the centre of the correlation interval, giving a centred time of $t_c = t + \tau/2$. Both t and t_c are given in figure 5 for reference.

Several key features of the net energy transfer over the correlation interval τ are observed in figure 5(c,d). First, the region in velocity space of largest net transfer

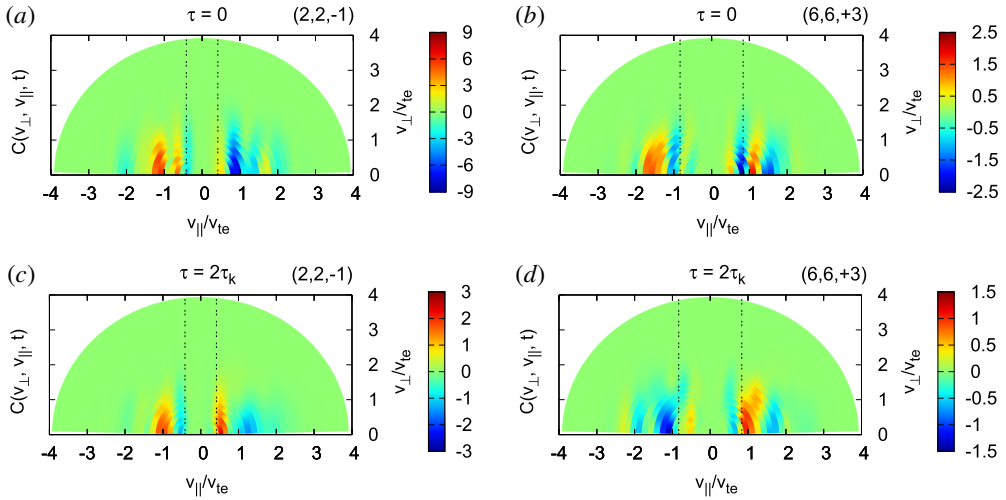


FIGURE 5. Electron gyrotropic correlation $C_{E_{\parallel}}(v_{\parallel}, v_{\perp}, t)$ for the $(2, 2, -1)$ Fourier mode using (a) $\tau = 0$ and (c) $\tau = 2\tau_k$, plotted at $t_c/\tau_0 = 0.86$, corresponding to $t/\tau_k = 0.81$ for $\tau = 2\tau_k$. Also plotted are $C_{E_{\parallel}}(v_{\parallel}, v_{\perp}, t)$ for the $(6, 6, +3)$ Fourier mode using (b) $\tau = 0$ and (d) $\tau = 2\tau_k$ at $t_c/\tau_0 = 0.34$, corresponding to $t/\tau_k = 0.42$ for $\tau = 2\tau_k$. Dashed lines denote Landau resonant velocities: $v_{p\parallel}/v_{te} = \pm 0.42$ for the $(2, 2, -1)$ Fourier mode and $v_{p\parallel}/v_{te} = \pm 0.84$ for the $(6, 6, +3)$ Fourier mode. Arbitrary units are used in the colour bars while the relative amplitudes between the $\tau = 0$ and $2\tau_k$ correlations are preserved for each Fourier mode.

of energy between E_{\parallel} and the electrons is closely connected to $v_{p\parallel}$. This contrasts with the broader spread over v_{\parallel} of instantaneous energy transfer when taking $\tau = 0$ in panels (a,b). The resulting velocity-space characteristic of the energy transfer is consistent with the velocity-space signature of Landau damping of the turbulent fluctuations, as found in previous studies (Klein & Howes 2016; Klein *et al.* 2017; Howes *et al.* 2017, 2018; Chen *et al.* 2019). The contrast in the energy transfer signals between the instantaneous and long-time-averaged correlations shows that while electrons over a broad range of parallel velocities participate in instantaneous energy transfer, the net secular energy transfer is largely contributed by ‘near-resonance’ electrons that are closely connected to $v_{p\parallel}$. This reflects the resonant nature of secular net energy transfer in Landau damping of the turbulent fluctuations. Second, the variation in the energy transfer is largely a function of v_{\parallel} , with weak v_{\perp} dependence other than the monotonic drop off as v_{\perp} increases. For the $(6, 6, +3)$ mode in (d) which has $k_{\perp}\rho_e \approx 1.7 > 1$, however, there is weak v_{\perp} dependence near $v_{\parallel}/v_{te} \sim 1$, which lasts very briefly, for $\sim 0.2\tau_k$. This v_{\perp} dependence in the energy transfer reveals structuring of the distribution in v_{\perp} as E_{\parallel} does not depend on velocity. This qualitative feature is consistent with the expectation of the electron entropy cascade (Schekochihin *et al.* 2009; Tatsuno *et al.* 2009; Schoeffler *et al.* 2014), which predicts some structuring of the distribution in v_{\perp} due to nonlinear phase mixing for $k_{\perp}\rho_e > 1$.

4.1.2. Ion gyrotropic correlations

In figure 6, we plot the instantaneous correlation $C_{E_{\parallel}}(\mathbf{k}, v_{\parallel}, v_{\perp}, t, \tau = 0)$ for ions for modes (a) $(1, 1, +3)$ and (b) $(2, 2, -1)$. As with the instantaneous correlations for

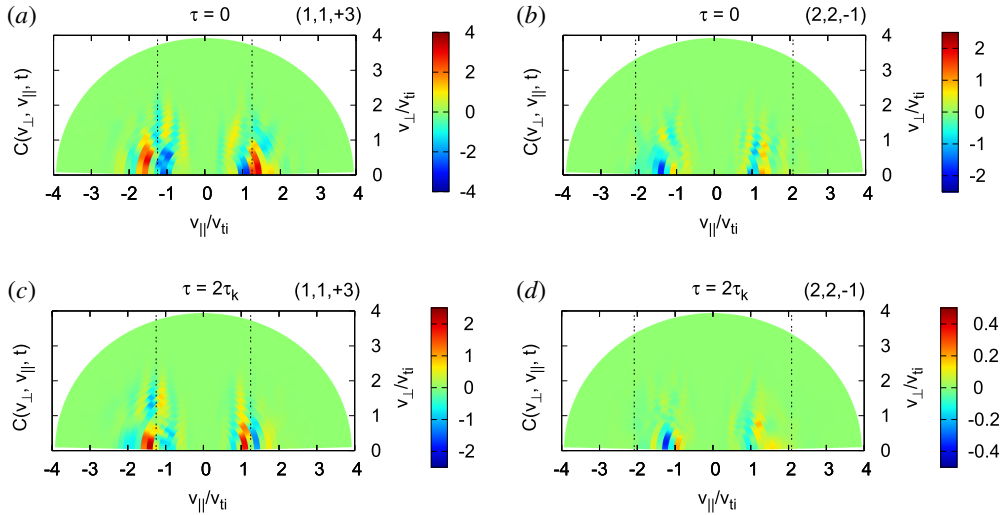


FIGURE 6. Ion gyrotropic correlation $C_{E_{\parallel}}(v_{\parallel}, v_{\perp}, t)$ for the $(1, 1, +3)$ Fourier mode using (a) $\tau = 0$ and (c) $\tau = 2\tau_k$, plotted at $t_c/\tau_0 = 1.2$, corresponding to $t/\tau_k = 0.48$ for $\tau = 2\tau_k$. (c) Shows observable weak v_{\perp} variations at $v_{\parallel} < 0$ in addition to more prominent v_{\parallel} dependence. Also plotted are $C_{E_{\parallel}}(v_{\parallel}, v_{\perp}, t)$ for the $(2, 2, -1)$ Fourier mode using (b) $\tau = 0$ and (d) $\tau = 2\tau_k$ at $t_c/\tau_0 = 0.90$, corresponding to $t/\tau_k = 0.90$ for $\tau = 2\tau_k$. Dashed lines denote Landau resonant velocities: $v_{p\parallel}/v_{ti} = \pm 1.3$ and ± 2.1 for the $(1, 1, +3)$ and $(2, 2, -1)$ Fourier modes, respectively. The same format is used as figure 5.

the electrons in figure 5, we see that the energy transfer is not tightly constrained in v_{\parallel} to the resonant parallel phase velocities for these modes ((a) $\omega/(k_{\parallel}v_{ti}) = \pm 1.2$ and (b) $\omega/(k_{\parallel}v_{ti}) = \pm 2.1$ (vertical dashed black lines)). For the $(2, 2, -1)$ mode, having resonant parallel phase velocities much higher than the ion thermal speed, there is only very weak energy transfer.

Computing the unnormalized correlation (time average) over the correlation interval $\tau = 2\tau_k$ for each mode, we obtain the ion energization rate in gyrotropic velocity space shown in figure 6 for Fourier modes (c) $(1, 1, +3)$ and (d) $(2, 2, -1)$. The ion energy transfer rate results for (c) $(1, 1, +3)$ have similar characteristics to the findings for the electrons: (i) the secular energy transfer rate is closely connected to the parallel resonant velocity; and (ii) the energy transfer rate varies strongly as a function of v_{\parallel} , again consistent with the velocity-space signature expected of Landau damping. One notable difference is that there is significantly more variation of the energy transfer rate in the v_{\perp} direction than for the electrons. This is qualitatively consistent with the action of the ion entropy cascade (Schekochihin *et al.* 2009; Tatsuno *et al.* 2009) which leads to structuring of the perturbed distribution function in the v_{\perp} direction (Howes 2008).

Another notable difference from the electron case is that the energy transfer rates are significantly weaker, with nearly no resonant energy transfer signatures near $v_{p\parallel}/v_{ti}$, for the (d) $(2, 2, -1)$ Fourier mode. In fact, the $(1, 1)$ Fourier modes are the only k_{\perp} value in the sampled spectrum (table 1) displaying resonant signatures in the resolved range of v_{\parallel}/v_{ti} plotted. The $(1, 1)$ Fourier modes also sit near the peak of the ion collisionless damping rate (γ_i in figure 1). At $k_{\perp}\rho_i > 2$, γ_i drops off rapidly. This is because $v_{p\parallel}/v_{ti}$ moves to the tail of the ion distribution (at greater than twice the ion thermal speed) where there are very few particles to interact with

the waves. For instance, the (2, 2) and (3, 4) Fourier modes have $v_{p\parallel}/v_{ti} = \pm 2.1$ and ± 3.3 , respectively, which are in the tail of the distribution. Indeed, resonant energy transfer signatures are not observed for the (2, 2) to (7, 7) Fourier modes.

4.2. Parallel reduced correlations

Because the variation of the rate of energy density transfer, shown in figures 5 and 6, is largely a function of v_{\parallel} with little variation in v_{\perp} , we may integrate over v_{\perp} to obtain reduced parallel correlations $C_{E_{\parallel}}(v_{\parallel}, t, \tau)$, given by (2.11). These reduced correlations can conveniently be plotted, for a given correlation interval τ , as timestack plots of $C_{E_{\parallel}}(v_{\parallel}, t)$ as a function of v_{\parallel} and time t to illustrate the evolution of the field–particle energy transfer due to a single Fourier mode over the course of the entire simulation.

4.2.1. Electron parallel reduced correlations

Plotted in figure 7 are timestack plots of the parallel reduced correlations $C_{E_{\parallel}}(v_{\parallel}, t)$ for the electrons for the (2, 2) Fourier mode, separately for each of the seven $k_z \in [-3, +3]$ modes in panels (a–g) and the sum of these seven k_z modes in panel (h), labelled (2, 2). The correlation interval chosen for all panels is $\tau = 2\tau_k$. Plotted to the right of each timestack plot is the v_{\parallel} -integrated correlation, giving the net transfer rate of energy density for that Fourier mode $\int C_{E_{\parallel}}(v_{\parallel}, t) dv_{\parallel}$ as a function of time (red curve) and the accumulated energy transferred $\int_0^t dt \int C_{E_{\parallel}}(v_{\parallel}, t) dv_{\parallel}$ over time (green curve). The Landau resonant parallel phase velocity of each Fourier mode is indicated by vertical black lines. We note that, for a given value of k_{\perp} , the normalized phase velocity $\bar{\omega} = \omega/k_{\parallel}v_A$ is independent of k_{\parallel} , so the phase velocity (ω/k_{\parallel}) is constant for all k_z (note that k_{\parallel} and k_z are the same in the linear dispersion relation by which $\bar{\omega}$ is given). This leads to a constant Landau resonant velocity, $v_{p\parallel}/v_{te} = \pm 0.42$, for all (2, 2, k_z) Fourier modes in figure 7. Also plotted on the right of the v_{\parallel} -integrated correlation for (h) the sum of the seven k_z mode is an axis for the normalized centred time t_c/τ_0 .

A key characteristic of the parallel reduced correlations for all (2, 2, k_z) Fourier modes is that the energy transfer is largely dominated by particles connected to $v_{p\parallel}$, with an increase in electron energy (red) just above $v_{p\parallel}$. This reduced parallel velocity-space signature is consistent with previous results showing Landau damping (Klein & Howes 2016; Klein *et al.* 2017; Howes *et al.* 2017, 2018; Chen *et al.* 2019). This localization of the energy transfer in parallel velocity indicates that collisionless damping by Landau resonant electrons is the dominant mechanism for transferring energy from the turbulent electromagnetic fluctuations to the electrons, a primary result of this study.

Furthermore, the timestack plots show clearly that this resonant energization of the electrons by the parallel electric field is sustained over the course of the simulation, although the amplitude of this rate of energization decreases in time as the initial fluctuations (the total turbulence energy) damp in time. In fact, the decrease in the rate of electron energization by the electric field over the course of the simulation is qualitatively consistent with the decrease in the spatially integrated rate of electron energization $\dot{E}_e^{(fp)}$ (solid blue) in figure 3(b). Additionally, the characteristic time scale of the energy transfer in the parallel reduced correlations is approximately τ_k of this (2, 2) Fourier mode. This time scale is consistent with the linear wave period of this Fourier mode, as naturally expected.

The panels (a–g) for the seven different (2, 2, k_z) Fourier modes in figure 7 show that most of the different k_z modes yield a net energy gain (green curve) at the end of

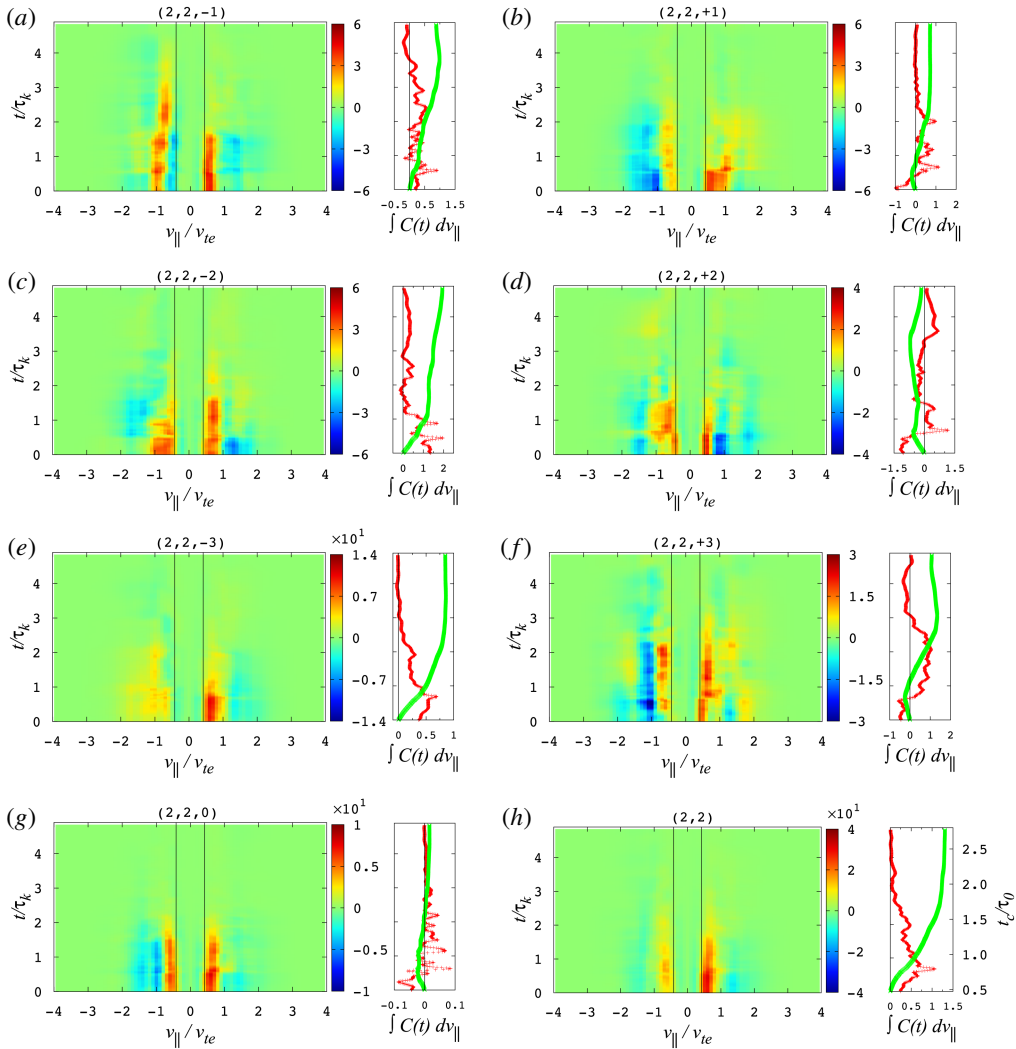


FIGURE 7. Electron parallel reduced correlations $C_{E\parallel}(v_{\parallel}, t)$ for seven k_z modes and summed $C_{E\parallel}(v_{\parallel}, t)$ for the (2, 2) Fourier mode. Correlation interval of $\tau = 2\tau_k$ is chosen. Time t is defined at the beginning of the correlation interval. Vertical black lines indicate Landau resonant velocities: $v_{p\parallel}/v_{te} = \pm 0.42$. An arbitrary unit is used. Line plots on the right of each correlation are the v_{\parallel} -integrated correlation as a function of time (red curve) and accumulated over time (green curve). The $\times 10^n$ factor above each colour bar applies also to the x -axis of the line plots. Also plotted on the right of panel (h) is an axis for the normalized centred time t_c/τ_0 .

the run. The (h) sum of these seven k_z components of the (2, 2) Fourier mode indeed demonstrates a net heating of electrons over the course of the simulation.

4.2.2. Ion parallel reduced correlations

In figure 8, we plot timestack plots of the parallel reduced correlations $C_{E\parallel}(v_{\parallel}, t)$ for the ions for the (1, 1) Fourier mode, in the same format as for the electrons

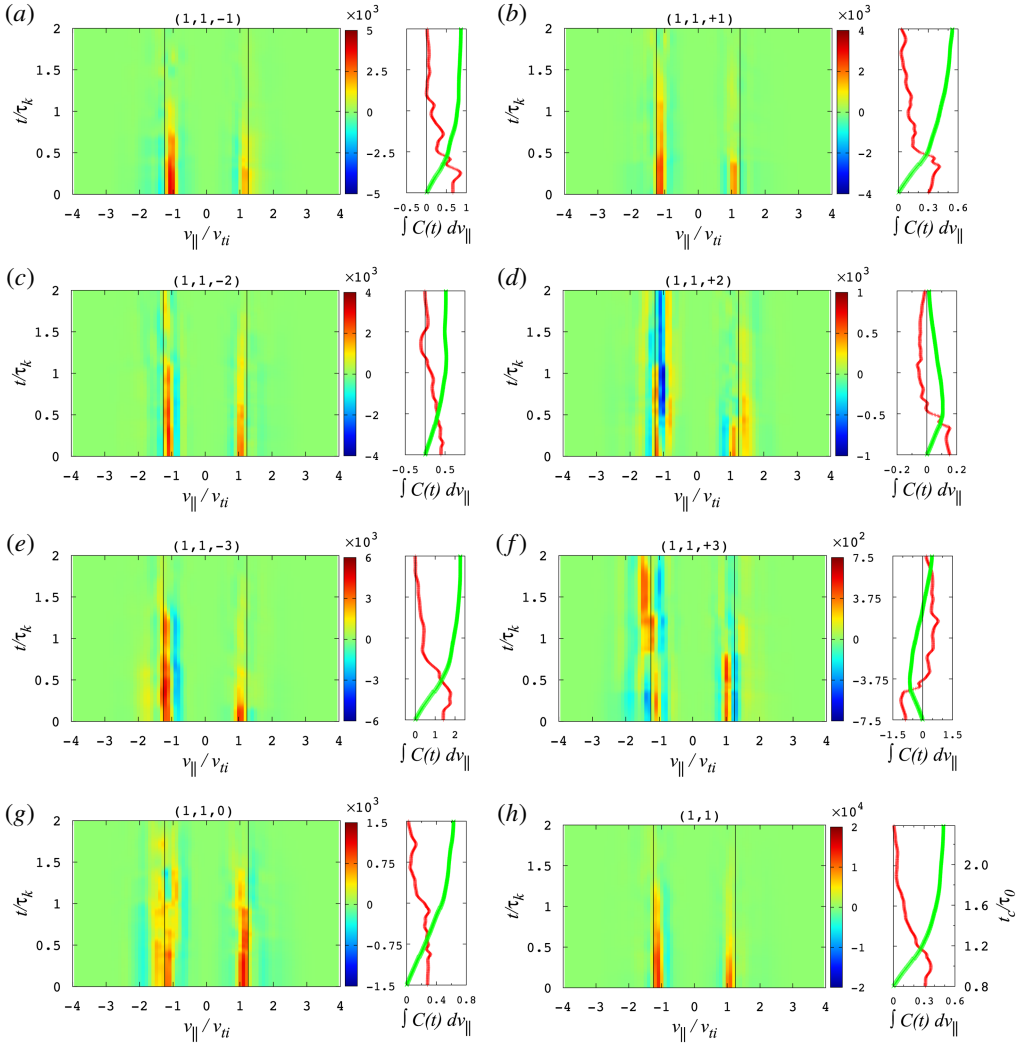


FIGURE 8. Ion parallel reduced correlations $C_{E\parallel}(v_{\parallel}, t)$ for seven k_z modes and summed $C_{E\parallel}(v_{\parallel}, t)$ for the (1, 1) Fourier mode. Correlation interval of $\tau = 2\tau_k$ is used. $C_{E\parallel}(v_{\parallel}, t)$ for each individual k_z mode shows resonant signatures associated with Landau resonances, $v_{p\parallel}/v_{ti} = \pm 1.3$, indicated by vertical black lines. Highly localized energy transfer signals are observed for all seven Fourier modes. The same format is used as figure 7. Arbitrary unit is used.

in figure 7. Again, a correlation interval of $\tau = 2\tau_k$ is used for all plots. The Landau resonant parallel phase velocity for these modes, normalized in terms of the ion thermal velocity, is given by $v_{p\parallel}/v_{ti} = \pm 1.3$.

The ion reduced parallel correlations for the (1, 1, k_z) modes also show that the energy transfer is largely dominated by particles near the resonant velocity, indicating that collisionless damping by Landau resonant ions is the dominant mechanism for transferring energy from the parallel electric field to the ions. Although there is significantly more variation of the accumulated energy transfer to the ions among the

different k_z modes in panels (a–g), the summed k_z result in (h) is also qualitatively consistent with the gradual decrease in time of the spatially integrated rate of ion energization $\dot{E}_i^{(fp)}$ (solid red) in figure 3(a). Furthermore, in the same way as the characteristic time scale of the electron energization rate being consistent with τ_k of the Fourier mode in figure 7, the characteristic time scale of the ion energization rate for the different k_z modes is also approximately τ_k of this (1, 1) Fourier mode.

Consistent with the rapid decrease of the ion collisionless damping rate $\gamma_i/k_{\parallel}v_A$ (cyan) in figure 2 at perpendicular wavenumbers $k_{\perp}\rho_i > 2$, the reduced parallel correlations (not shown) for all Fourier modes other than (1, 1) do not exhibit clear resonant energy transfer velocity-space signatures.

4.2.3. Reduced parallel correlations: k_{\perp} dependence and β_i dependence

Previous applications of the field-particle correlation have analysed the energy transfer at a single point in space (Klein & Howes 2016; Klein *et al.* 2017; Howes *et al.* 2017, 2018; Chen *et al.* 2019). Although this has the advantage of enabling the spatial localization of the energy transfer between fields and particles to be studied, it cannot provide any information about how that energy transfer is mediated by fluctuations at different scales. By performing the field-particle correlation analysis in Fourier space, we can examine how the energy transfer as a function of the scale of the Fourier modes plays a role in the energy transfer. In the gyrokinetic limit $k_{\parallel} \ll k_{\perp}$, the resonant parallel phase velocity ω/k_{\parallel} of the kinetic Alfvén wave modes is strictly a function of $k_{\perp}\rho_i$ (as shown in figure 1a), so the reduced parallel correlation for a single perpendicular wavevector (k_x, k_y) summed over k_z has a single resonant velocity. We may obtain a clean velocity-space signature for each distinct $k_{\perp}\rho_i$ mode.

In figure 9, we present timestack plots of the reduced parallel correlations for the electrons summed over the seven k_z modes for each diagnosed k_{\perp} case spanning $1.4 \leq k_{\perp}\rho_i \leq 9.9$, or $0.3 \leq k_{\perp}\rho_e \leq 2$. The same format as the summed- k_z results in figure 7(h) is used. The results clearly show the distinct advantages of the Fourier implementation of the field-particle correlation technique. First, the energy transfer signal for different $k_{\perp}\rho_i$ modes follows closely the increasing Landau resonant velocity (vertical black lines) as $k_{\perp}\rho_i$ increases from (a) through (f). A net energy energization of the electrons is obtained in all of $k_{\perp}\rho_i$ modes, as shown in the accumulated energy transferred (green curve). Clearly, Landau resonant interactions with the electrons must play a key role in the damping of fluctuations across the sampled range of scales, consistent with expectations for a significant rate of collisionless damping by the electrons, $\gamma_e/\omega_{A0} \gtrsim O(0.1)$, as shown in figure 1(b). Second, the magnitude of energy transfer drops by approximately 3 orders of magnitude from $k_{\perp}\rho_i = 1.4$ to $k_{\perp}\rho_i = 9.9$. Of course, the number of perpendicular Fourier modes increases linearly with k_{\perp} , so the decrease in amplitude with $k_{\perp}\rho_i$ is partly compensated by the larger number of Fourier modes at higher $k_{\perp}\rho_i$. Nonetheless, the first one or two $k_{\perp}\rho_i$ modes that we diagnosed here (specifically $k_{\perp}\rho_i = 1.4$ and $k_{\perp}\rho_i = 2.8$) would dominate the signals in a single-point diagnostic, so one would not be able to identify the energy transfer mediated by higher $k_{\perp}\rho_i$ modes without Fourier decomposition. Finally, the characteristic time scale of the energy transfer is consistent with τ_k of each (k_x, k_y) Fourier mode, even though τ_k decreases with increasing $k_{\perp}\rho_i$. As seen in the accumulated energy transferred (green curve), most of the electron energization

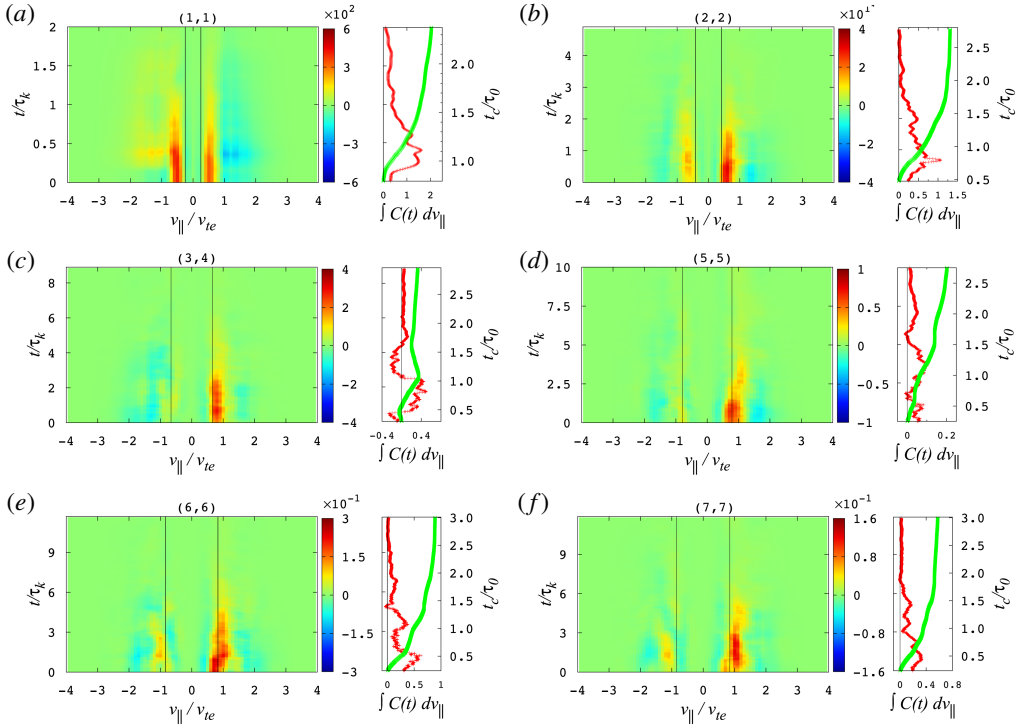


FIGURE 9. Parallel reduced correlations summed over seven k_z modes $\sum_{k_z=-3}^3 C_{E_{\parallel}}(v_{\parallel}, t)$ for 6 (k_x, k_y) values: (1, 1), (2, 2), (3, 4), (5, 5), (6, 6) and (7, 7), representing a total of 42 Fourier modes of electron parallel reduced correlations. Their Landau resonant velocities are: $v_{p\parallel}/v_{te} = \pm(0.25, 0.42, 0.66, 0.79, 0.84, 0.85)$ respectively. The same format is used as figure 7(h).

occurs before a normalized centred time of $t_c/\tau_0 \sim 1.5$. This is consistent with the spatially integrated rate of electron energization $\dot{E}_e^{(fp)}$ (solid blue) in figure 3(b) being the most significant by $1.5\tau_0$.

In order to illustrate more clearly how the energy transfer to the electrons closely tracks that Landau resonant velocity of kinetic Alfvén waves with a given perpendicular wavenumber $k_{\perp}\rho_i$, we zoom into the central part of the v_{\parallel} range in figure 10(a–c). The localized region dominating electron energization moves to higher v_{\parallel} with higher $k_{\perp}\rho_i$, consistent with the increasing resonant parallel phase velocity of kinetic Alfvén waves as k_{\perp} increases. This analysis strongly suggests that collisionless damping via the Landau resonance with electrons plays a key role in the removal of energy from the turbulence and consequent energization of the electrons.

Another plasma parameter that has a strong impact on the resonant parallel phase velocity of kinetic Alfvén waves is the plasma β_i . We performed simulations with an identical set-up as the $\beta_i = 1$ simulation described in § 2.5, but with values $\beta_i = 0.1$ and $\beta_i = 0.01$. To analyse both of these additional simulations, we take a correlation interval $\tau = \tau_k$ for the (2, 2, –1) mode analysed here. In figure 10(d–f), we present timestack plots of the reduced parallel correlation $C_{E_{\parallel}}(v_{\parallel}, t, \tau)$ for electrons for Fourier mode (2, 2, –1). The resonant parallel phase velocity $v_{p\parallel}$ for the (2, 2) Fourier mode,

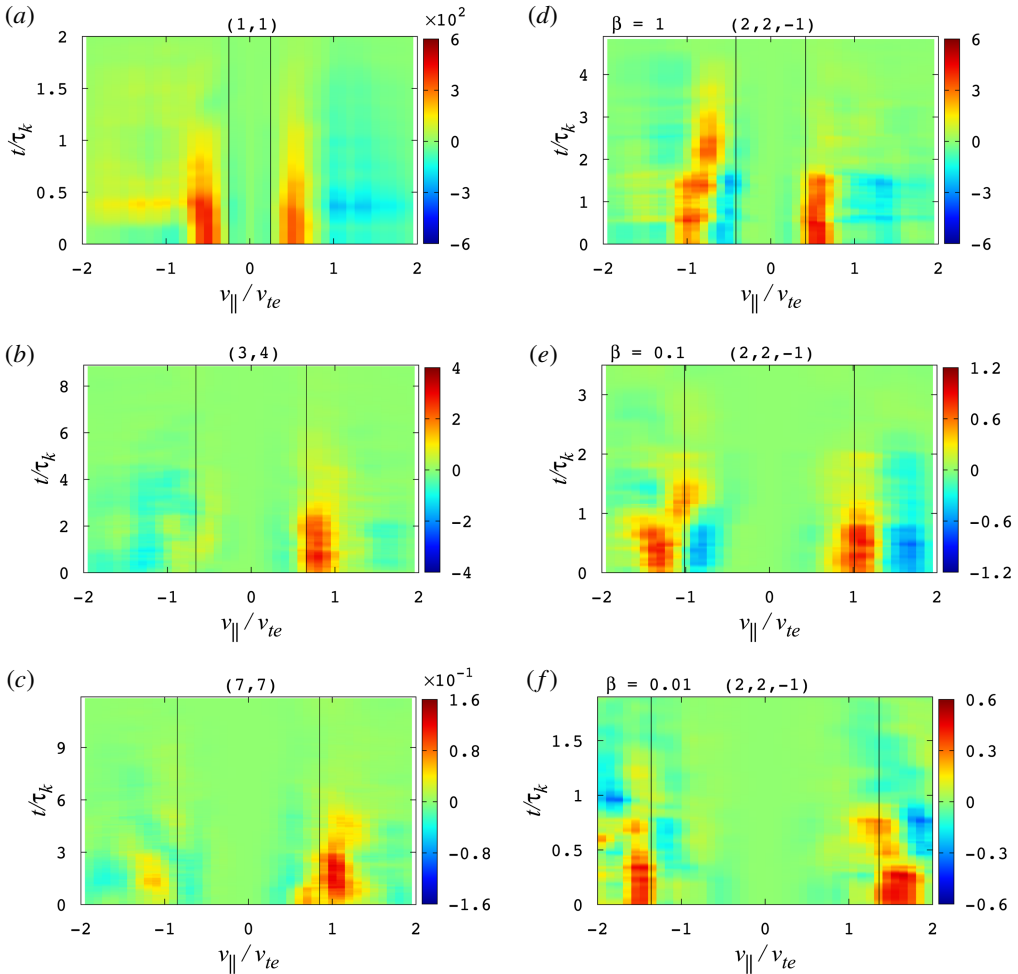


FIGURE 10. (a–c) Zoomed-in plot of summed- k_z correlations from figure 9 for 3 (k_x, k_y) values – (1, 1), (3, 4) and (7, 7) with the corresponding Landau resonant velocities being $v_{p\parallel}/v_{te} = \pm(0.25, 0.66, 0.85)$, respectively – showing how the field–particle energy transfer rate closely tracks the resonant parallel phase velocities as (k_x, k_y) increases. (d–f) Electron parallel reduced correlations $C_{E\parallel}(v_{\parallel}, t)$ for the (2, 2, –1) Fourier mode from simulations with $\beta_i = 1$ (current run), 0.1 and 0.01 in which the Landau resonant velocity, $v_{p\parallel}/v_{te} = \pm(0.42, 1.0, 1.4)$, respectively, increases with decreasing β_i . The energy transfer signals from all three simulations show remarkable agreement with the increasing parallel resonant velocity.

when normalized to v_{te} , increases with values $\omega/(k_{\parallel} v_{te}) = \pm 0.42, \pm 1.0, \pm 1.4$ (vertical black lines) as the values of β_i decreases for these three simulations $\beta_i = 1, 0.1, 0.01$. We indeed find a remarkably close association between $v_{p\parallel}$ and the region of velocity space where the electrons participate in energy exchange with the parallel electric field E_{\parallel} . This close quantitative agreement with the β_i dependence of phase velocities observed in the simulations again suggests the dominant role that the Landau resonance plays in the field–particle energy transfer for electrons in the turbulence systems.

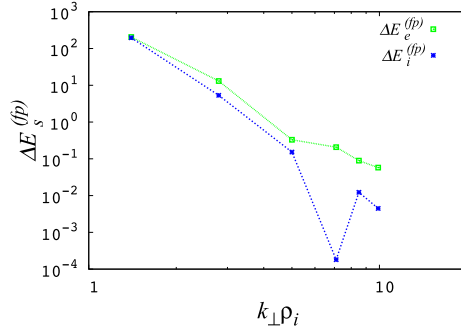


FIGURE 11. Accumulated particle energization $\Delta E_s^{(fp)}$ at the end of the simulation for the sampled (k_x, k_y) modes (summed over k_z) as a function of $k_{\perp} \rho_i$. Each (k_x, k_y) mode is represented by a point and all points are connected by lines. The same normalization is used for both ion $\Delta E_i^{(fp)}$ (blue) and electron $\Delta E_e^{(fp)}$ (green) energization.

4.2.4. Accumulated particle energization: k_{\perp} dependence

The collisionless field–particle energy transfer rate is directly measured by the field–particle correlations. With the sampled Fourier spectrum, we can see how the accumulated particle energization varies as a function of the length scales of the fluctuations. In figure 11, we plot this accumulated particle energization at the end of the simulation $\Delta E_s^{(fp)}$ as a function of $k_{\perp} \rho_i$. Each point represents the accumulated energization in each (k_x, k_y) Fourier mode summed over k_z for ions (blue) and electrons (green). The electron energization $\Delta E_e^{(fp)}$ is then the value of the green curve at the end of the simulation for each (k_x, k_y) mode in figure 9. The same normalization is used for both ion and electron energization, $\Delta E_i^{(fp)}$ and $\Delta E_e^{(fp)}$.

Several features of $\Delta E_s^{(fp)}$ are notable. First, the particle energization is dominated by the lowest k_{\perp} mode that has the strongest amplitude, as expected. Second, the total ion and electron energization over the sampled spectrum are comparable given that both species are nearly equally energized at this dominant, lowest k_{\perp} mode. This is consistent with the comparable species heating rates due to field–particle interactions $\dot{E}_s^{(fp)}$ (solid) in figure 3 in the turbulence system². This is also consistent with the ion and electron collisionless damping rates, γ_i and γ_e , being of the same order of magnitude at $k_{\perp} \rho_i \sim 1$, represented by the lowest k_{\perp} mode, in figure 1. Third, when plotted as a function of $k_{\perp} \rho_i$, $\Delta E_s^{(fp)}$ here can represent the energy transfer spectra; for electrons, $\Delta E_e^{(fp)}$ indicates a spectral rollover at the electron gyroradius scale of $k_{\perp} \rho_e = 1$ ($k_{\perp} \rho_i = 5$), becoming less steep at $k_{\perp} \rho_e > 1$. Lastly, ion energization shows a dip at $k_{\perp} \rho_i = 7$, rather than a monotonic drop for all $k_{\perp} \rho_i \geq 7$ modes as would be expected from the ion collisionless damping rate, suggesting that collisionless damping cannot completely explain ion energization. These interesting features deserve further investigation in the future.

5. Conclusions

The field–particle correlation technique is a new method both for determining the rate of transfer of energy between electromagnetic fields and plasma particles and

²Note that in order to use the field–particle correlations to quantitatively measure the total species heating (that is approximately twice larger for the electrons than for the ions), energization from the whole system and hence all possible Fourier modes needs to be taken into account.

for identifying the physical mechanisms responsible for that energy transfer through their velocity-space signatures. Previous implementations of this novel technique employ a time series of the particle velocity distribution and electromagnetic field measurements performed at a single point in space. Here, we present an alternative Fourier implementation of the field–particle correlation technique that determines the energy transfer for a single wavevector in Fourier space instead of at a single point in physical space.

The Fourier implementation has the capability to explore the energy transfer between fields and particles as a function of the length scale of the fluctuations, information that cannot be obtained through single-point measurements in physical space. Furthermore, in a broadband turbulent spectrum, the resonant parallel phase velocity ω/k_{\parallel} is generally a function of the wavevector, resonant collisionless interactions analysed in terms of Fourier wavevector modes are expected to yield a clean velocity-space signature at the resonant velocity. This contrasts the single-point implementation in which all wave modes will contribute to the energy transfer at a given point, potentially smearing out the velocity-space signals over the range of resonant velocities for all contributing wave modes. Furthermore, the Fourier decomposition separates the contributions to the energy transfer from each scale, enabling the energy transfer for small amplitude modes at high wavenumber to be observed even in the presence of much larger amplitude modes at lower wavenumbers. This contrasts with the single-point implementation in which the much larger amplitude modes at lower wavenumbers will dominate the energy transfer. Finally, in the Fourier implementation, the correlation intervals need only extend over a few periods of the mode under investigation, even in the presence of larger amplitude, lower-frequency modes.

The Fourier implementation employs information throughout the spatial domain to decompose fluctuations as a function of scale, so it cannot be applied to analyse spacecraft observations that provide measurements at only one, or possibly a few, points in space. Nonetheless, it can be used in numerical simulations in which full spatial information is accessible. The key advantage of the Fourier implementation to investigate the particle energization as a function of the length scale of the electromagnetic fluctuations provides insights that are complementary to the spatial information of particle energization provided by the more standard, single-point implementation. In fact, dual implementation of the field–particle correlation technique in both physical and Fourier space in simulations can take the advantages of both approaches in identifying collisionless energy transfer in simulations supporting spacecraft missions.

Here we apply the Fourier implementation of the field–particle correlation technique to investigate the energization of the ions and electrons in strong electromagnetic turbulence. We simulate a 3-D extension of the standard Orszag–Tang vortex (3-D OTV) problem, a set-up previously used to explore the differences between 2-D and 3-D turbulence (Li *et al.* 2016). We follow the flow of energy in the simulation from turbulent energy that is first collisionlessly transferred to particles as non-thermal energy in the velocity distribution functions of the ions and electrons, and later is collisionally thermalized to ion and electron heat. For the $\beta_i = 1$ conditions of the simulation, we find that the electrons are heated about twice as much as the ions. We show that the particle energization in the simulation, equal to $\mathbf{J} \cdot \mathbf{E}$ integrated over the simulation volume, occurs in a spatially non-uniform manner, with the dominant

heating confined to narrow current sheet layers associated with strong parallel electric fields.

Applying the Fourier implementation of the field–particle correlation technique to the simulation, we find that the velocity-space signature of electron and ion energization for a particular Fourier mode is consistent with Landau damping at the resonant parallel phase velocity of the kinetic Alfvén wave for that mode. Timestack plots of the electron and ion energization by the parallel electric field E_{\parallel} also show a net energization of the plasma particles at the expense of the turbulent energy.

The regions of velocity space in which particles exchange energy with the electric field closely follow the resonant parallel phase velocity for kinetic Alfvén waves as the perpendicular wavenumber k_{\perp} and plasma β_i are varied (figure 10). This shows that collisionless damping via the Landau resonance with ions and electrons is an important channel of particle energization in strong electromagnetic turbulence, relevant to space plasmas, such as the solar corona, solar wind and planetary magnetospheres.

Acknowledgements

T.C.L. is grateful to T. Parashar, N. Loureiro, K. Schoeffler and A. Mallet for valuable discussions. Supported by NSF CAREER Award AGS-1054061, NASA grants 80NSSC18K0754, 80NSSC18K0289, 80NSSC18K0643, 80NSSC18K1217 and 80NSSC18K1371, NASA HSR grant NNX16AM23G, and NSF SHINE award AGS-1622306. Computations used the Extreme Science and Engineering Discovery Environment (XSEDE), which is supported by NSF grant ACI-1053575.

Appendix. Determination and significance of correlation interval

Here we illustrate how a sufficiently long correlation interval is determined and its significance using electron parallel reduced correlations, which conveniently depict the energy transfer rate as a function of v_{\parallel} and time t . Plotted in figure 12 are electron parallel reduced correlations for a correlation interval $\tau = 0, 0.5\tau_k, \tau_k$ and $2\tau_k$ for the $(2, 2, -1)$ Fourier mode in (a)–(d).

Using $\tau = 0$, (a) the instantaneous energy transfer between E_{\parallel} and electrons manifests as alternating red and blue signals over short time scales as they exchange energy back and forth many times throughout the course of the simulation. As τ increases in (b) through (d), the time evolution of the energy transfer becomes increasingly concentrated to $v_{p\parallel}$. In (c,d), the time evolution of the energy transfer begins to be qualitatively consistent, with mostly red signals just above $v_{p\parallel}$. The maximum amplitude of energy transfer for $\tau = \tau_k$ and $2\tau_k$ in (c,d) becomes comparable, whereas it is reduced by over twice from (a) $\tau = 0$ to (b) $\tau = 0.5\tau_k$. This indicates that a correlation interval of $\tau \geq \tau_k$ leads to a qualitative convergence of the time evolution of the energy transfer rate as a function of v_{\parallel} . Hence, $\tau \geq \tau_k$ represents a sufficiently long correlation interval. The choice of $\tau = 2\tau_k$ used in this work is suitable for capturing the net secular energy transfer signals in velocity space.

An important feature again illustrated in figure 12 is that while electrons over a broad range of v_{\parallel} participate in (a) the instantaneous energy transfer, the secular net energy transfer identified by correlating over a suitably long time period in (c,d) is dominated by ‘near-resonance’ electrons that are close to the parallel resonant velocity $v_{p\parallel}$.

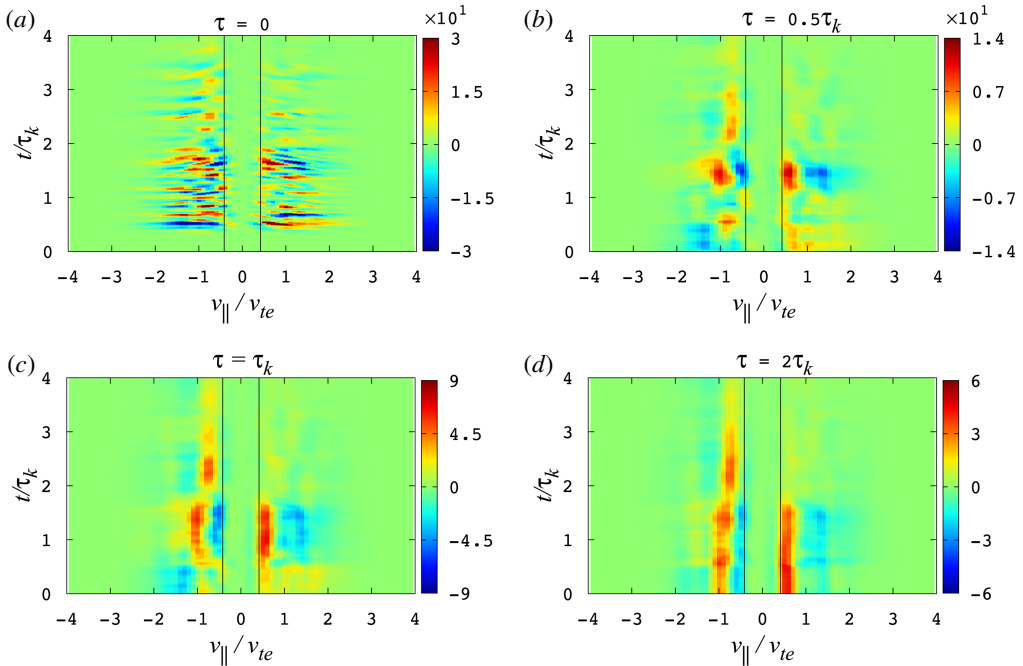


FIGURE 12. Electron parallel reduced correlations $C_{E_{\parallel}}(v_{\parallel}, t)$ using a correlation interval (a) $\tau = 0$, (b) $\tau = 0.5\tau_k$, (c) $\tau = \tau_k$ and (d) $\tau = 2\tau_k$ for the $(2, 2, -1)$ Fourier mode. The Landau resonant velocities: $v_{p\parallel}/v_{te} = \pm 0.42$, are indicated by vertical black lines. Time t is defined at the beginning of the correlation interval.

REFERENCES

- ABEL, I. G., BARNES, M., COWLEY, S. C., DORLAND, W. & SCHEKOCHIHIN, A. A. 2008 Linearized model Fokker–Planck collision operators for gyrokinetic simulations. I. Theory. *Phys. Plasmas* **15** (12), 122509; [arXiv:0808.1300](https://arxiv.org/abs/0808.1300).
- ADKINS, T. & SCHEKOCHIHIN, A. A. 2018 A solvable model of vlasov-kinetic plasma turbulence in fourierhermite phase space. *J. Plasma Phys.* **84** (1), 905840107.
- ALEXANDROVA, O., CHEN, C. H. K., SORRISO-VALVO, L., HORBURY, T. S. & BALE, S. D. 2013 Solar wind turbulence and the role of ion instabilities. *Space Sci. Rev.* **178**, 101–139; [arXiv:1306.5336](https://arxiv.org/abs/1306.5336).
- ARZAMASSKIY, L., KUNZ, M. W., CHANDRAN, B. D. G. & QUATAERT, E. 2019 Hybrid-kinetic simulations of ion heating in Alfvénic turbulence. *Astrophys. J.* **53**; doi:[10.3847/1538-4357/ab20cc](https://doi.org/10.3847/1538-4357/ab20cc).
- BARNES, A. 1966 Collisionless damping of hydromagnetic waves. *Phys. Fluids* **9**, 1483–1495.
- BARNES, M., ABEL, I. G., DORLAND, W., ERNST, D. R., HAMMETT, G. W., RICCI, P., ROGERS, B. N., SCHEKOCHIHIN, A. A. & TATSUNO, T. 2009 Linearized model Fokker–Planck collision operators for gyrokinetic simulations. II. Numerical implementation and tests. *Phys. Plasmas* **16** (7), 072107.
- BOLDYREV, S., HORAITES, K., XIA, Q. & PEREZ, J. C. 2013 Toward a theory of astrophysical plasma turbulence at subproton scales. *Astrophys. J.* **777**, 41.
- BRIZARD, A. J. & HAHM, T. S. 2007 Foundations of nonlinear gyrokinetic theory. *Rev. Mod. Phys.* **79**, 421–468.
- BURCH, J. L., MOORE, T. E., TORBERT, R. B. & GILES, B. L. 2016 Magnetospheric multiscale overview and science objectives. *Space Sci. Rev.* **199** (1), 5–21.

- CERRI, S. S., KUNZ, M. W. & CALIFANO, F. 2018 Dual phase-space cascades in 3d hybrid-*vlavosmaxwell* turbulence. *Astrophys. J. Lett.* **856** (1), L13.
- CHANDRAN, B. D. G., LI, B., ROGERS, B. N., QUATAERT, E. & GERMASCHEWSKI, K. 2010 Perpendicular ion heating by low-frequency Alfvén-wave turbulence in the solar wind. *Astrophys. J.* **720**, 503–515.
- CHANG, O., PETER GARY, S. & WANG, J. 2014 Energy dissipation by whistler turbulence: three-dimensional particle-in-cell simulations. *Phys. Plasmas* **21** (5), 052305.
- CHEN, C. H. K., BOLDYREV, S., XIA, Q. & PEREZ, J. C. 2013 Nature of subproton scale turbulence in the solar wind. *Phys. Rev. Lett.* **110** (22), 225002; [arXiv:1305.2950](https://arxiv.org/abs/1305.2950).
- CHEN, C. H. K., KLEIN, K. G. & HOWES, G. G. 2019 Evidence for electron Landau damping in space plasma turbulence. *Nat. Commun.* **10**, 740 [arXiv:1902.05785](https://arxiv.org/abs/1902.05785).
- CHEN, L., LIN, Z. & WHITE, R. 2001 On resonant heating below the cyclotron frequency. *Phys. Plasmas* **8**, 4713–4716.
- COLEMAN, P. J. JR. 1968 Turbulence, viscosity, and dissipation in the solar-wind plasma. *Astrophys. J.* **153**, 371–388.
- DAHLBURG, R. B. & PICONE, J. M. 1989 Evolution of the Orszag–Tang vortex system in a compressible medium. I – Initial average subsonic flow. *Phys. Fluids B* **1**, 2153–2171.
- DAHLIN, J. T., DRAKE, J. F. & SWISDAK, M. 2016 Parallel electric fields are inefficient drivers of energetic electrons in magnetic reconnection. *Phys. Plasmas* **23** (12), 120704.
- FRANCI, L., LANDI, S., MATTEINI, L., VERDINI, A. & HELLINGER, P. 2015 High-resolution hybrid simulations of kinetic plasma turbulence at proton scales. *Astrophys. J.* **812** (1), 21.
- FRIEMAN, E. A. & CHEN, L. 1982 Nonlinear gyrokinetic equations for low-frequency electromagnetic waves in general plasma equilibria. *Phys. Fluids* **25**, 502–508.
- GERSHMAN, D. J., F-VIÑAS, A., DORELLI, J. C., BOARDSEN, S. A., AVANOV, L. A., BELLAN, P. M., SCHWARTZ, S. J., LAVRAUD, B., COFFEY, V. N., CHANDLER, M. O. *et al.* 2017 Wave-particle energy exchange directly observed in a kinetic Alfvén-branch wave. *Nat. Commun.* **8**, 14719.
- GOLDREICH, P. & SRIDHAR, S. 1995 Toward a theory of interstellar turbulence II. Strong Alfvénic turbulence. *Astrophys. J.* **438**, 763–775.
- GRAUER, R. & MARLIANI, C. 2000 Current-sheet formation in 3D ideal incompressible magnetohydrodynamics. *Phys. Rev. Lett.* **84**, 4850.
- GROŚELJ, D., CERRI, S. S., NAVARRO, A. B., WILLMOTT, C., TOLD, D., LOUREIRO, N. F., CALIFANO, F. & JENKO, F. 2017 Fully kinetic versus reduced-kinetic modeling of collisionless plasma turbulence. *Astrophys. J.* **847** (1), 28.
- GROŚELJ, D., CHEN, C. H. K., MALLET, A., SAMTANEY, R., SCHNEIDER, K. & JENKO, F. 2018 Kinetic turbulence in astrophysical plasmas: waves and/or structures? Preprint, [arXiv:1806.05741](https://arxiv.org/abs/1806.05741).
- HE, J., TU, C., MARSCH, E. & YAO, S. 2012 Do oblique Alfvén/Ion-cyclotron or fast-mode/whistler waves dominate the dissipation of solar wind turbulence near the proton inertial length? *Astrophys. J. Lett.* **745**, L8.
- HOWES, G. G. 2008 Inertial range turbulence in kinetic plasmas. *Phys. Plasmas* **15** (5), 055904.
- HOWES, G. G. 2015 A dynamical model of plasma turbulence in the solar wind. *Phil. Trans. R. Soc. Lond. A* **373** (2041), 20140145.
- HOWES, G. G. 2016 The dynamical generation of current sheets in astrophysical plasma turbulence. *Astrophys. J. Lett.* **82**, L28 [arXiv:1607.07465](https://arxiv.org/abs/1607.07465).
- HOWES, G. G. 2017 A prospectus on kinetic heliophysics. *Phys. Plasmas* **24** (5), 055907; [arXiv:10.1063/1.4983993](https://arxiv.org/abs/10.1063/1.4983993).
- HOWES, G. G., COWLEY, S. C., DORLAND, W., HAMMETT, G. W., QUATAERT, E. & SCHEKOCHIHIN, A. A. 2006 Astrophysical gyrokinetics: basic equations and linear theory. *Astrophys. J.* **651**, 590–614; [arXiv:astro-ph/0511812](https://arxiv.org/abs/astro-ph/0511812).
- HOWES, G. G., COWLEY, S. C., DORLAND, W., HAMMETT, G. W., QUATAERT, E. & SCHEKOCHIHIN, A. A. 2008a A model of turbulence in magnetized plasmas: implications for the dissipation range in the solar wind. *J. Geophys. Res.* **113** (A12), A05103; [arXiv:0707.3147](https://arxiv.org/abs/0707.3147).

- HOWES, G. G., DORLAND, W., COWLEY, S. C., HAMMETT, G. W., QUATAERT, E., SCHEKOCIHIN, A. A. & TATSUNO, T. 2008b Kinetic simulations of magnetized turbulence in astrophysical plasmas. *Phys. Rev. Lett.* **100** (6), 065004.
- HOWES, G. G., KLEIN, K. G. & LI, T. C. 2017 Diagnosing collisionless energy transfer using fieldparticle correlations: Vlasovpoisson plasmas. *J. Plasma Phys.* **83** (1), 705830102.
- HOWES, G. G., MCCUBBIN, A. J. & KLEIN, K. G. 2018 Spatially localized particle energization by landau damping in current sheets produced by strong alfvén wave collisions. *J. Plasma Phys.* **84** (1), 905840105.
- HOWES, G. G., TENBARGE, J. M., DORLAND, W., QUATAERT, E., SCHEKOCIHIN, A. A., NUMATA, R. & TATSUNO, T. 2011 Gyrokinetic simulations of solar wind turbulence from ion to electron scales. *Phys. Rev. Lett.* **107**, 035004.
- HUGHES, R. S., GARY, S. P., WANG, J. & PARASHAR, T. N. 2017 Kinetic alfvén turbulence: electron and ion heating by particle-in-cell simulations. *Astrophys. J. Lett.* **847** (2), L14.
- ISENBERG, P. A. & HOLLWEG, J. V. 1983 On the preferential acceleration and heating of solar wind heavy ions. *J. Geophys. Res.* **88**, 3923–3935.
- KARIMABADI, H., ROYTERSHTEYN, V., WAN, M., MATTHAEUS, W. H., DAUGHTON, W., WU, P., SHAY, M., LORING, B., BOROVSKY, J., LEONARDIS, E. *et al.* 2013 Coherent structures, intermittent turbulence, and dissipation in high-temperature plasmas. *Phys. Plasmas* **20** (1), 012303.
- KAWAZURA, Y., BARNES, M. & SCHEKOCIHIN, A. A. 2019 Thermal disequilibrium of ions and electrons by collisionless plasma turbulence. *Proc. Natl Acad. Sci.* **116**, 771–776; [arXiv:1807.07702](https://arxiv.org/abs/1807.07702).
- KLEIN, K. G. 2017 Characterizing fluid and kinetic instabilities using field–particle correlations on single-point time series. *Phys. Plasmas* **24** (5), 055901.
- KLEIN, K. G. & HOWES, G. G. 2016 Measuring collisionless damping in heliospheric plasmas using fieldparticle correlations. *Astrophys. J. Lett.* **826** (2), L30.
- KLEIN, K. G., HOWES, G. G. & TENBARGE, J. M. 2017 Diagnosing collisionless energy transfer using fieldparticle correlations: gyrokinetic turbulence. *J. Plasma Phys.* **83** (4), 535830401.
- KOBAYASHI, S., ROGERS, B. N. & NUMATA, R. 2014 Gyrokinetic simulations of collisionless reconnection in turbulent non-uniform plasmas. *Phys. Plasmas* **21** (4), 040704.
- KRUSKAL, M. D. & OBERMAN, C. R. 1958 On the stability of plasma in static equilibrium. *Phys. Fluids* **1**, 275–280.
- LANDAU, L. D. 1946 On the vibrations of the electronic plasma. *Zh. Eksp. Teor. Fiz.* **16**, 574.
- LI, T. C., HOWES, G. G., KLEIN, K. G. & TENBARGE, J. M. 2016 Energy dissipation and landau damping in two- and three-dimensional plasma turbulence. *Astrophys. J. Lett.* **832** (2), L24.
- MININNI, P. D., POUQUET, A. G. & MONTGOMERY, D. C. 2006 Small-scale structures in three-dimensional magnetohydrodynamic turbulence. *Phys. Rev. Lett.* **97** (24), 244503; [arXiv:physics/0607269](https://arxiv.org/abs/physics/0607269).
- MORRISON, P. J. 1994 The energy of perturbations for Vlasov plasmas. *Phys. Plasmas* **1**, 1447–1451.
- NARITA, Y., GARY, S. P., SAITO, S., GLASSMEIER, K.-H. & MOTSCHMANN, U. 2011 Dispersion relation analysis of solar wind turbulence. *Geophys. Res. Lett.* **38**, L05101.
- NARITA, Y., NAKAMURA, R., BAUMJOHANN, W., GLASSMEIER, K.-H., MOTSCHMANN, U., GILES, B., MAGNES, W., FISCHER, D., TORBERT, R. B., RUSSELL, C. T. *et al.* 2016 On electron-scale whistler turbulence in the solar wind. *Astrophys. J. Lett.* **827** (1), L8.
- NAVARRO, A. B. N., TEACA, B., TOLD, D., GROSELJ, D., CRANDALL, P. & JENKO, F. 2016 Structure of plasma heating in gyrokinetic alfvénic turbulence. *Phys. Rev. Lett.* **117**, 245101.
- NIELSON, K. D., HOWES, G. G. & DORLAND, W. 2013 Alfvén wave collisions, the fundamental building block of plasma turbulence. II. Numerical solution. *Phys. Plasmas* **20** (7), 072303; [arXiv:1306.1456](https://arxiv.org/abs/1306.1456).
- NUMATA, R., DORLAND, W., HOWES, G. G., LOUREIRO, N. F., ROGERS, B. N. & TATSUNO, T. 2011 Gyrokinetic simulations of the tearing instability. *Phys. Plasmas* **18** (11), 112106; [arXiv: 1107.5842](https://arxiv.org/abs/1107.5842).
- NUMATA, R., HOWES, G. G., TATSUNO, T., BARNES, M. & DORLAND, W. 2010 AstroGK: astrophysical gyrokinetics code. *J. Comput. Phys.* **229**, 9347 [arXiv:1004.0279](https://arxiv.org/abs/1004.0279).

- NUMATA, R. & LOUREIRO, N. F. 2015 Ion and electron heating during magnetic reconnection in weakly collisional plasmas. *J. Plasma Phys.* **81**, 3001 [arXiv:1406.6456](https://arxiv.org/abs/1406.6456).
- ORSZAG, S. A. & TANG, C.-M. 1979 Small-scale structure of two-dimensional magnetohydrodynamic turbulence. *J. Fluid Mech.* **90**, 129–143.
- PARASHAR, T. N. & MATTHAEUS, W. H. 2016 Proximity of current and vortex structures: effects on collisionless plasma heating. *Astrophys. J.* **832** (1), 57.
- PARASHAR, T. N., SHAY, M. A., CASSAK, P. A. & MATTHAEUS, W. H. 2009 Kinetic dissipation and anisotropic heating in a turbulent collisionless plasma. *Phys. Plasmas* **16** (3), 032310.
- PARASHAR, T. N., VASQUEZ, B. J. & MARKOVSKII, S. A. 2014 The role of electron equation of state in heating partition of protons in a collisionless plasma. *Phys. Plasmas* **21** (2), 022301.
- PASSOT, T. & SULEM, P. L. 2015 A model for the non-universal power law of the solar wind sub-ion-scale magnetic spectrum. *Astrophys. J. Lett.* **812** (2), L37.
- PERRONE, D., ALEXandroVA, O., MANGENEY, A., MAKSIMOVIC, M., LACOMBE, C., RAKOTO, V., KASPER, J. C. & JOVANOVIĆ, D. 2016 Compressive coherent structures at ion scales in the slow solar wind. *Astrophys. J.* **826** (2), 196.
- PICONE, J. M. & DAHLBURG, R. B. 1991 Evolution of the Orszag–Tang vortex system in a compressible medium. II. Supersonic flow. *Phys. Fluids B* **3**, 29–44.
- POLITANO, H., POUQUET, A. & SULEM, P. L. 1989 Inertial ranges and resistive instabilities in two-dimensional magnetohydrodynamic turbulence. *Phys. Fluids B* **1**, 2330–2339.
- POLITANO, H., POUQUET, A. & SULEM, P. L. 1995 Current and vorticity dynamics in three-dimensional magnetohydrodynamic turbulence. *Phys. Plasmas* **2**, 2931–2939.
- QUATAERT, E. 1998 Particle heating by Alfvénic turbulence in hot accretion flows. *Astrophys. J.* **500**, 978–991; [arXiv:astro-ph/9710127](https://arxiv.org/abs/astro-ph/9710127).
- ROBERTS, O. W., ALEXandroVA, O., KAJDI, P., TURC, L., PERRONE, D., ESCOUBET, C. P. & WALSH, A. 2017 Variability of the magnetic field power spectrum in the solar wind at electron scales. *Astrophys. J.* **850** (2), 120.
- ROBERTS, O. W., LI, X. & JESKA, L. 2015 A statistical study of the solar wind turbulence at ion kinetic scales using the k -filtering technique and cluster data. *Astrophys. J.* **802**, 2.
- ROBERTS, O. W., LI, X. & LI, B. 2013 Kinetic plasma turbulence in the fast solar wind measured by cluster. *Astrophys. J.* **769**, 58 [arXiv:1303.5129](https://arxiv.org/abs/1303.5129).
- SAHRAOUI, F., GOLDSTEIN, M. L., BELMONT, G., CANU, P. & REZEAU, L. 2010 Three dimensional anisotropic k spectra of turbulence at subproton scales in the solar wind. *Phys. Rev. Lett.* **105** (13), 131101.
- SCHEKOCHIHIN, A. A., COWLEY, S. C., DORLAND, W., HAMMETT, G. W., HOWES, G. G., PLUNK, G. G., QUATAERT, E. & TATSUNO, T. 2008 Gyrokinetic turbulence: a nonlinear route to dissipation through phase space. *Plasma Phys. Control. Fusion* **50** (12), 124024; [arXiv:0806.1069](https://arxiv.org/abs/0806.1069).
- SCHEKOCHIHIN, A. A., COWLEY, S. C., DORLAND, W., HAMMETT, G. W., HOWES, G. G., QUATAERT, E. & TATSUNO, T. 2009 Astrophysical Gyrokinetics: kinetic and fluid turbulent cascades in magnetized weakly collisional plasmas. *Astrophys. J. Suppl.* **182**, 310–377.
- SCHEKOCHIHIN, A. A., KAWAZURA, Y. & BARNES, M. A. 2019 Constraints on ion versus electron heating by plasma turbulence at low beta. *J. Plasma Phys.* **85** (3), 905850303; [arXiv:1812.09792](https://arxiv.org/abs/1812.09792).
- SCHEKOCHIHIN, A. A., PARKER, J. T., HIGHCOCK, E. G., DELLAR, P. J., DORLAND, W. & HAMMETT, G. W. 2016 Phase mixing versus nonlinear advection in drift-kinetic plasma turbulence. *J. Plasma Phys.* **82** (2), 905820212.
- SCHOEFFLER, K. M., LOUREIRO, N. F., FONSECA, R. A. & SILVA, L. O. 2014 Magnetic-field generation and amplification in an expanding plasma. *Phys. Rev. Lett.* **112** (17), 175001; [arXiv:1308.3421](https://arxiv.org/abs/1308.3421).
- SERVIDIO, S., CHASAPIS, A., MATTHAEUS, W. H., PERRONE, D., VALENTINI, F., PARASHAR, T. N., VELTRI, P., GERSHMAN, D., RUSSELL, C. T., GILES, B. *et al.* 2017 Magnetospheric multiscale observation of plasma velocity-space cascade: Hermite representation and theory. *Phys. Rev. Lett.* **119**, 205101.

- TATSUNO, T., SCHEKOCIHIN, A. A., DORLAND, W., PLUNK, G., BARNES, M. A., COWLEY, S. C. & HOWES, G. G. 2009 Nonlinear phase mixing and phase-space cascade of entropy in gyrokinetic plasma turbulence. *Phys. Rev. Lett.* **103** (1), 015003.
- TENBARGE, J. M., DAUGHTON, W., KARIMABADI, H., HOWES, G. G. & DORLAND, W. 2014 Collisionless reconnection in the large guide field regime: Gyrokinetic versus particle-in-cell simulations. *Phys. Plasmas* **21** (2), 020708.
- TENBARGE, J. M. & HOWES, G. G. 2012 Evidence of critical balance in kinetic Alfvén wave turbulence simulations. *Phys. Plasmas* **19** (5), 055901.
- TENBARGE, J. M. & HOWES, G. G. 2013 Current sheets and collisionless damping in kinetic plasma turbulence. *Astrophys. J. Lett.* **771**, L27 [arXiv:1304.2958](https://arxiv.org/abs/1304.2958).
- TENBARGE, J. M., HOWES, G. G. & DORLAND, W. 2013 Collisionless damping at electron scales in solar wind turbulence. *Astrophys. J.* **774**, 139.
- TOLD, D., JENKO, F., TENBARGE, J. M., HOWES, G. G. & HAMMETT, G. W. 2015 Multiscale nature of the dissipation range in gyrokinetic simulations of Alfvénic turbulence. *Phys. Rev. Lett.* **115** (2), 025003; [arXiv:1505.02204](https://arxiv.org/abs/1505.02204).
- VÁSCONEZ, C. L., VALENTINI, F., CAMPOREALE, E. & VELTRI, P. 2014 Vlasov simulations of kinetic alfvén waves at proton kinetic scales. *Phys. Plasmas* **21** (11), 112107.
- VECH, D., KLEIN, K. G. & KASPER, J. C. 2017 Nature of stochastic ion heating in the solar wind: testing the dependence on plasma beta and turbulence amplitude. *Astrophys. J. Lett.* **850** (1), L11.
- WAN, M., MATTHAEUS, W. H., ROYTERSHEYN, V., PARASHAR, T. N., WU, P. & KARIMABADI, H. 2016 Intermittency, coherent structures and dissipation in plasma turbulence. *Phys. Plasmas* **23** (4), 042307.
- WANG, X., TU, C.-Y., HE, J.-S. & WANG, L.-H. 2018 Ion-scale spectral break in the normal plasma beta range in the solar wind turbulence. *J. Geophys. Res.* **123** (1), 68–75.
- YANG, Y., MATTHAEUS, W. H., PARASHAR, T. N., HAGGERTY, C. C., ROYTERSHEYN, V., DAUGHTON, W., WAN, M., SHI, Y. & CHEN, S. 2017 Energy transfer, pressure tensor, and heating of kinetic plasma. *Phys. Plasmas* **24** (7), 072306.